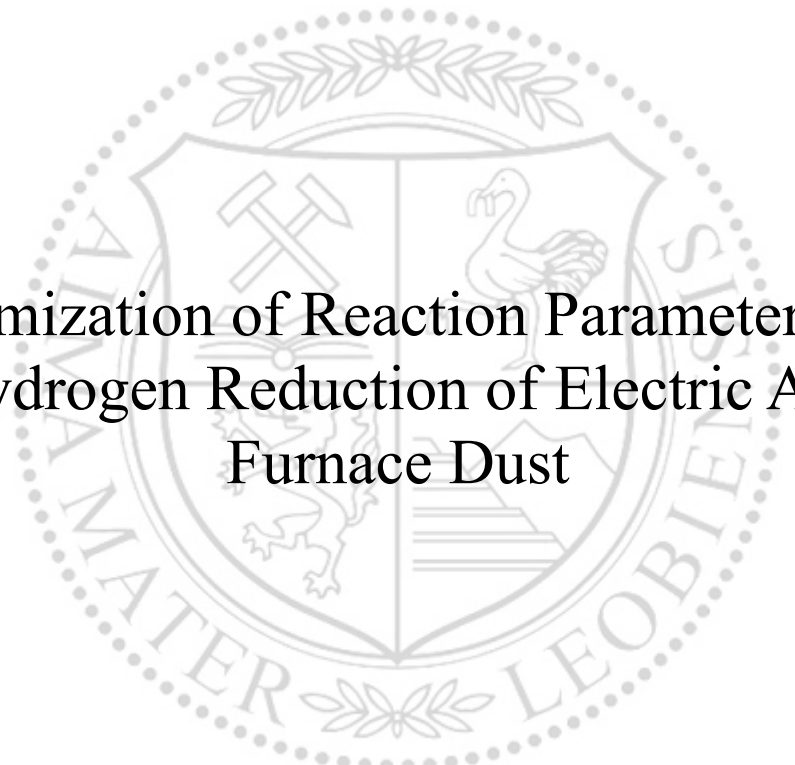




Chair of Nonferrous Metallurgy

Master's Thesis



Optimization of Reaction Parameters for
Hydrogen Reduction of Electric Arc
Furnace Dust

Aaron Fabian Keuschnig, BSc

May 2024



EIDESSTATTLICHE ERKLÄRUNG

Ich erkläre an Eides statt, dass ich diese Arbeit selbstständig verfasst, andere als die angegebenen Quellen und Hilfsmittel nicht benutzt, den Einsatz von generativen Methoden und Modellen der künstlichen Intelligenz vollständig und wahrheitsgetreu ausgewiesen habe, und mich auch sonst keiner unerlaubten Hilfsmittel bedient habe.

Ich erkläre, dass ich den Satzungsteil „Gute wissenschaftliche Praxis“ der Montanuniversität Leoben gelesen, verstanden und befolgt habe.

Weiters erkläre ich, dass die elektronische und gedruckte Version der eingereichten wissenschaftlichen Abschlussarbeit formal und inhaltlich identisch sind.

Datum 13.05.2024



Unterschrift Verfasser/in
Aaron Fabian Keuschnig

Acknowledgments

Ich möchte mich herzlich bei meinen Eltern bedanken, die es mir ermöglicht haben zu studieren und mich während des gesamten Studiums stets unterstützt haben. Dank ihrer Hilfe konnte ich mich nicht nur akademisch, sondern auch persönlich weiterentwickeln. Ein großer Dank gilt auch meinen Großeltern, die mir stets mit unendlichem Verständnis begegnet sind. Mein Bruder hat mir in den letzten Jahren emotionalen Halt gegeben – dafür bin ich ihm sehr dankbar!

Auch meinen Freund:innen in der Heimat möchte ich danken! Trotz des selteneren Kontakts in den letzten Jahren habe ich nie das Gefühl gehabt, dass unsere Freundschaft an Wert verloren hat.

Ohne meine Freundschaften hier in Leoben hätte ich mein Studium wahrscheinlich nicht erfolgreich abschließen können. Sie haben mich stets unterstützt und mir geholfen, wenn es mal nicht so gut lief - besonders in den letzten Jahren.

Zu guter Letzt möchte ich mich noch bei meinem Betreuer, Manuel Leuchtenmüller, bedanken. Er hat mir die Forschung nähergebracht und mich in den letzten neun Monaten intensiv unterstützt.

Abstract

The recycling of galvanized scrap generates a zinc-containing dust fraction, usually called Electric Arc Furnance Dust EAFD, which is currently mainly treated in the carbon-based Waelz process. While the process is efficient in terms of zinc-recovery and process economy, it produces a secondary zinc concentrate with a large carbon footprint and underutilizes other valuable elements that are present in the EAFD. Climate change mitigation efforts require the substitution of carbon-based processes with carbon-neutral alternatives, such as hydrogen.

To achieve this objective, it is important to have a fundamental understanding of the reaction kinetics of the reduction reactions with hydrogen. The present work investigates the influence of the temperature and H_2O/H_2 ratio on the reaction kinetics during the EAFD reduction. Experiments were conducted in a Thermogravimetric Analyzer TGA that was coupled with a Mass Spectrometer MS. The second objective was to develop an algorithm, that allows to distinguish between the reduction of zinc-oxide and iron-oxide by coupling the TGA and MS datasets.

Experimental data demonstrated a full recovery of zinc (> 99 %) within a 60-minute hydrogen reduction period. The remaining solid material, which can be described as secondary-grade direct reduced iron (DRI), exhibited a high degree of metallization and a high iron concentration (> 70 %). Up to 1.150 °C, the reaction kinetics increased with the temperature. Above this point, the reactivity of the material decreased rapidly. During the reduction, the material shrinkage increased within reaction temperatures of 900-1.050 °C, but stagnated above that temperature. Interestingly, the H_2O/H_2 ratio of the atmosphere influenced the shrinkage behavior. A higher H_2O concentration in the gas led to a higher material shrinkage. In contrast, the reaction kinetics decreased with higher H_2O concentrations.

The influence of the process parameters on the reaction kinetics of the EAFD could be identified. Additionally, the experimental setup was optimized to facilitate further investigations of the reaction kinetics.

Kurzfassung

Beim Recycling von verzinktem Schrott fällt eine zinkhaltige Staubfraktion an, die in der Regel als Stahlwerksstaub bezeichnet wird und derzeit hauptsächlich im kohlenstoffbasierten Wälzprozess aufgearbeitet wird. Dieses Verfahren ist in Bezug auf die Zink-Rückgewinnungsrate effizient und weist niedrige Betriebskosten auf, wodurch es auch wirtschaftlich erfolgreich ist. Dabei zielt der Wälzprozess lediglich auf die Extraktion von Zink ab, weshalb andere Wertmetalle, allen voran Eisen und Kupfer, ungenutzt bleiben. Außerdem weist das im Wälzprozess gewonnene sekundäre Zinkoxid einen hohen CO₂-Fußabdruck auf, was aufgrund verstärkter Klimaschutzbemühungen in Zukunft die Entwicklung von Alternativverfahren erforderlich macht, die das kohlenstoffbasierte Verfahren durch Alternativen, wie die Wasserstoffreduktion, ersetzen.

Bei der Entwicklung neuer Verfahrenskonzepte ist es wichtig, ein grundlegendes Verständnis der ablaufenden Reaktionsmechanismen sowie der Reaktionskinetik zu haben. Die vorliegende Arbeit leistet hier einen Beitrag, wobei der Einfluss der Temperatur und des H_2O/H_2 -Verhältnisses auf die Reaktionskinetik während der wasserstoffbasierten Reduktion von Stahlwerksstaub untersucht wurde. Dazu wurden Experimente in einer Thermogravimetrie (TGA) durchgeführt, die mit einem Massenspektrometer (MS) gekoppelt war. Ergänzend war geplant, einen Algorithmus zu entwickeln, der es ermöglicht, durch Kopplung der TGA- und MS-Datensätze quantitativ zwischen der Reduktion von Zinkoxid und Eisenoxid zu unterscheiden.

Die experimentellen Daten zeigen, dass mittels Wasserstoffreduktion innerhalb von 60 Minuten eine nahezu vollständige (> 99 %) Rückgewinnung von Zink erfolgt. Der verbleibende Feststoff hat eine hohe Eisenkonzentration (> 70 %) und erreicht einen hohen Metallisierungsgrad, wodurch er als Schrottersatz in der Lichtbogenofenroute einsetzbar ist. Bis zu 1.150 °C steigt die Reaktionskinetik mit zunehmender Temperatur an. Oberhalb davon nimmt die Reaktivität aufgrund von ausgeprägten Sintereffekten stark ab. Während des Reduktionsprozesses schrumpfte das Material im Bereich von 900 bis 1.050 °C mit steigender Temperatur stärker, darüber hinaus stagnierte die Volumenabnahme. Interessanterweise beeinflusste das H_2O/H_2 -Verhältnis der Atmosphäre das Schrumpfungsverhalten ebenfalls. Eine höhere H_2O -Konzentration im Gas führte zu einer höheren Volumenabnahme. Im Gegensatz dazu nahm die Reaktionskinetik mit steigender H_2O -Konzentration ab.

Der Einfluss der Reaktionsparameter auf die Reduktionskinetik konnte identifiziert werden. Des Weiteren wurde der experimentelle Aufbau weiter optimiert, um zukünftige Untersuchungen zur Reaktionskinetik zu erleichtern.

Contents

1	Introduction	1
1.1	Electric arc furnace dust	2
1.1.1	Formation	2
1.1.2	Characterization	3
1.2	Recovery of electric arc furnace dust	5
1.2.1	Waelz process	5
2	Experimental Procedure	8
2.1	Setup and data preparation	8
2.1.1	Sample preparation	9
2.1.2	Thermogravimetric analyzer	10
2.1.3	Data preparation	12
2.2	Process parameter study	14
2.2.1	Reproducibility of the experiments	14
2.2.2	Experimental evaluation	16
2.3	Quantitative influence of process parameters on the reaction kinetics	25
2.3.1	Methodology	25
2.3.2	Gas model of the TGA reactor	30
2.3.3	Results applying a single continuous stirred tank reactor	32
2.3.4	Results applying a series of continuous stirred tank reactors	33
2.3.5	The complex mixing behavior of the gas in the reactor	35
3	Summary and Outlook	38
	Bibliography	41
	List of Figures	44
	List of Tables	45

1 Introduction

Climate change is often referred to as the biggest challenge of the 21st century, and its consequences have prompted governments worldwide to take decisive action. The primary cause of climate change is the substantial increase in greenhouse gas emissions into the atmosphere since the 18th century Industrial Revolution. Notable examples of greenhouse gases are carbon dioxide, methane, nitrogen oxides, and halogenated compounds, which have the characteristic of trapping infrared rays emitted from the Earth's surface, thereby increasing the energy retention of the planet. This accumulation influences the energy balance of the Earth, leading to a temperature rise. To assess the impact of each individual gas on climate change, emission metrics like the global warming potential have been developed. The global warming potential measures the heat a kilogram of a gas traps over 100 years relative to carbon dioxide, expressed as carbon dioxide equivalents, making the impact of different greenhouse gases comparable [1]. In 2019, global greenhouse gas emissions reached approximately 50 billion tons of carbon dioxide equivalents, with an increasing trend [2]. In response, the European Commission launched the European Green Deal, aiming for a carbon-neutral European Union by 2050 and decoupling economic growth from resource use [3]. The iron and steel industry is responsible for around 7.2 % of the carbon dioxide emissions worldwide [4]. Therefore, there is a lot of pressure on this industry to reduce greenhouse gas emissions and substitute carbon-based processes. Many research projects investigate hydrogen-based reduction processes as a sustainable alternative to conventional carbon-based processes [5, 6, 7, 8, 9]. But it is not only the industrial sector transitioning towards hydrogen. It is also a key component in power and heat generation, energy storage and to some extent in the transportation sector [10]. Therefore, hydrogen will be a demanded raw material and energy carrier in the future [11]. It is therefore important to produce hydrogen economically in the required quantities and expand its infrastructure for distribution and storage [12].

To efficiently use hydrogen as a reducing agent in the metallurgical industry, an understanding of the fundamental reaction mechanisms and kinetics is crucial. This master thesis is a contribution to the *Dust2Value* project, which is funded by the EU Horizon Europe funding framework. The aim of the project is to develop a novel methodology for the extraction of zinc oxide from Electric Arc Furnance Dust EAFD, a waste in steelmaking via the Electric Arc Furnace EAF route, to technology readiness level 5. The conventional method for recycling EAFD involves a carbon-based treatment process to recover zinc oxide, which is associated with a high carbon footprint of the produced secondary-grade crude zinc oxide and the generation of underutilized slag [13, 14]. The *Dust2Value* process seeks to mitigate these carbon dioxide emissions by substituting carbon as a reducing agent for the reduction of the zinc oxide with hydrogen. For a successful process development, a fundamental understanding of the ongoing reaction mechanisms, the influence of reaction parameters and the reaction rate limiting reaction steps is important. Therefore, this work will investigate the influence of temperature and gas composition on the reaction kinetics and the shrinkage behavior of the EAFD during a hydrogen-based reduction treatment.

To develop a kinetic database, the training data should not only include the overall mass loss rate, but also reaction rates for iron and zinc oxide as a function of process parameters. Therefore, the objective of the second part of this work is to develop a methodology to distinguish between the reduction of zinc and iron oxide.

1.1 Electric arc furnace dust

Steel scrap is recycled within the EAF route, where it is melted in an EAF. Galvanized steel scrap that is filled into the EAF does not only contain steel, but also zinc. During the EAF steelmaking, a dust fraction usually named EAFD is generated and captured within the furnace off-gas system via bag filters. For every ton of produced steel, 15 to 23 kg of EAFD accumulates [13]. Considering the overall crude steel production via the EAF route in 2021, 564 Mt of steel [15] were produced leading to an EAFD generation of around 8.5 - 13 Mt [15]. The majority of the EAFD consists of zinc and iron oxides, but also contains leachable heavy metal compounds like lead, cadmium or chromium. A typical range for the zinc concentration is 20 - 25 wt.-% resulting in around 1.7 - 3.3 Mt of zinc to be recovered from this secondary source¹.

1.1.1 Formation

To understand the formation of EAFD it is important to have a basic knowledge about the processes inside the EAF. The main aggregate of the EAF is the furnace with its graphite electrodes. After the furnace is filled up with scrap, an electric arc occurs between the electrodes and the scrap, heating and melting it via radiation. Fig. 1 gives an overview of the furnace chamber of an EAF.

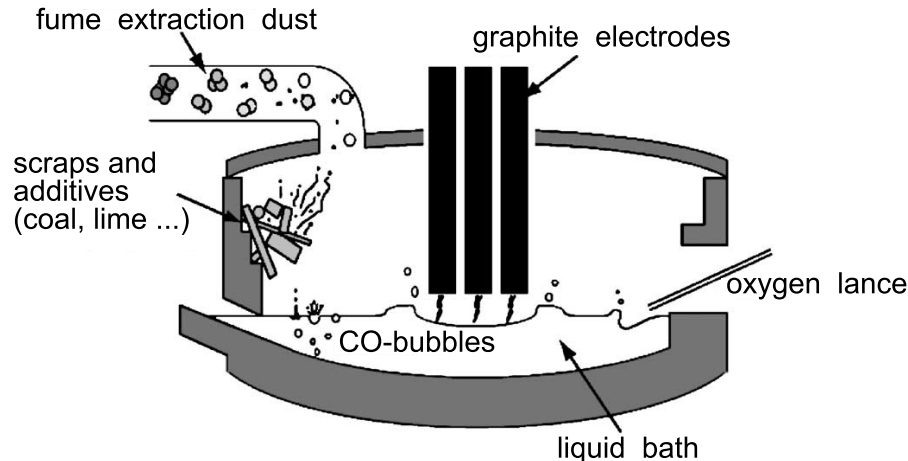


Fig. 1: Schematic illustration of the EAF [16]

Zinc accumulates in the EAFD as it volatilizes due to its high vapor pressure at the high process temperature of around 1,600 °C [17]. This mechanism removes practically all zinc from the liquid steel. After it volatilizes it is carried out by the exhaust gas flow. During that process, it cools down and re-oxidizes with oxygen to form zinc oxide. The dust consists of fine particles with most grains below 1 µm, however, due to agglomeration, the small particles form larger ones within the off-gas stream [18].

The electric arc reaches high temperatures, leading to a high heat loss due to radiation. To reduce that heat loss from radiation, carbon powder with oxygen is injected via lances to produce a so-called foamy slag. The foam covers the surface area of the liquid bath

¹Andreas Ruh, Befesa, Daten aus Europa

and the electric arc itself. As a result, it lowers the heat loss due to radiation. However, when the foam bubbles burst, particles shoot out of the slag and are to some extent sucked in by the off-gas system. Fig. 2 shows the two formation steps of dust via bubble bursting. As the bubble rises up to the surface of the liquid bath (a), it lifts up a liquid film, that gets thinner due to drainage. At some point, the film is too thin to prevent the bubble from rising out of the liquid bath and it bursts (b), leaving many small droplets called film drops. These are the first type of droplet that forms in this process. The other mechanism is when the liquid fills the cavity of the gas bubble and creates an upward Rayleigh jet that tears up into many droplets called jet drops. Guezennec et al. claim that up to 60% of dust particles are generated by this mechanism [16].

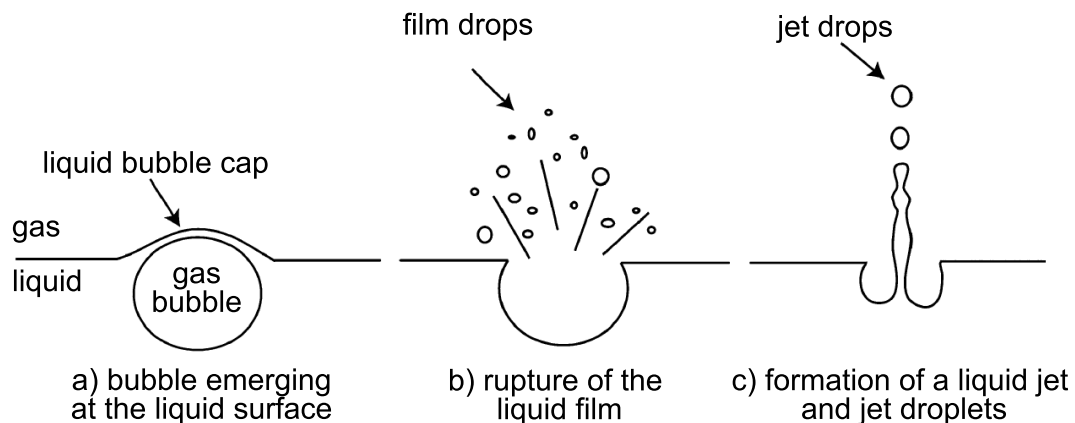


Fig. 2: Schematic representation of the burst of a bubble on a liquid surface [16]

Another dust formation mechanism is the so-called carry over, that occurs during the charging of either scrap or slag additives. Especially slag additives contain fine particles that are light enough to be carried out by the exhaust gas flow.

Additionally to the mechanisms mentioned above, the turbulence caused by the electric arc and the oxygen lance also lead to a projection of droplets at the impact points. The exhaust gas coming from the furnace is subsequently cooled down and the EAFD in it is separated by a bag house filter.

1.1.2 Characterization

As the composition of the EAFD is strongly dependent on the scrap used in the steelmaking process, there is significant variation between different steel plants and even within the same steel plant over time.

Composition

The major components of EAFD are iron oxide and zinc oxide. The zinc in the scrap is introduced into the dust mainly from galvanized parts of the scrap. During the EAF steelmaking process, additives are added to the scrap to optimize the process. One such additive is lime, which is used to remove phosphorus from the steel. More problematic elements in the EAFD are chlorides, sulfur, lead, chromium, and cadmium, as some of them are leachable. Chlorides are introduced into the EAFD by coatings and paints on the scrap. Lead is mainly brought into the dust via solder joints. Chromium is a widely used alloy element in steelmaking.

Depending on the investigated EAFD, the zinc content ranges from 2–15 % to 28–46 % [17, 19, 20]. As seen in Tab. 1, the zinc concentration fluctuates significantly over time even within the same plant [20]. Stathopoulos et al. investigated the EAFD of a steel mill in Greece and took samples of the dust on eleven consecutive days. Columns that did not vary significantly were merged. The last two columns were added to the table to provide the average concentration and the Coefficient of Variation CV of each substance. The CV shows the standard deviation of each substance over the eleven samples normalized by their mean value. A high CV indicates high variation between the samples, whereas a low CV indicates a more constant concentration. As seen in Tab. 1, only chloride shows a low CV, meaning it varies less, while the concentrations of the other substances fluctuate more.

Sample	Day 1-4	Day 5	Day 6	Day 7	Day 8-10	Day 11	Mean	CV
ZnO	30.62	21.34	33.69	33.36	19.11	35.13	27.58	0.23
Fe ₂ O ₃	13.49	5.55	18.91	16.74	33.57	15.60	19.23	0.49
CaO	9.42	9.91	4.66	3.69	7.88	8.60	8.02	0.31
PbO	6.78	3.28	6.47	6.01	5.20	6.37	5.89	0.19
Cl ⁻	5.00	4.31	4.87	4.98	4.39	4.91	4.75	0.07
SiO ₂	3.77	8.39	3.96	3.58	4.68	NaN	4.50	0.31
SO ₄ ²⁻	4.05	12.05	3.98	4.59	2.17	3.88	4.29	0.61
Na ₂ O	3.32	5.80	2.83	2.85	3.73	1.40	3.40	0.30
K ₂ O	2.96	2.07	3.21	2.77	2.40	1.66	2.61	0.20
NiO	1.76	2.69	2.29	1.75	3.74	0.03	2.27	0.49
MgO	1.59	2.78	1.44	1.33	1.95	1.53	1.75	0.27
Al ₂ O ₃	1.67	2.49	0.81	0.69	1.77	1.77	1.61	0.50
MnO	1.34	1.84	1.52	1.09	1.39	0.82	1.35	0.20
CuO	0.32	0.20	0.35	0.34	0.36	0.30	0.32	0.16
Cr ₂ O ₃	0.26	0.23	0.29	0.24	0.22	0.28	0.25	0.15
CdO	0.09	0.03	0.15	0.13	0.05	0.15	0.09	0.44
F ⁻	0.07	0.21	0.07	0.05	0.06	0.07	0.08	0.64
CoO	0.01	0.01	0.01	0.01	0.01	0.01	0.01	0.00

Tab. 1: Composition of EAFD samples from a steel mill on eleven consecutive days [20]

The zinc in the EAFD is present in the form of zincite (ZnO) and franklinite (ZnFe₂O₄), whereas most of the iron is in the form of hematite (Fe₂O₃) [19] or magnetite (Fe₃O₄) [17] or franklinite (ZnFe₂O₄).

Environmental aspects

EAFD is considered one of the most critical wastes in the steelmaking industry, as it also contains leachable, toxic elements like lead, chloride, cadmium, and chromium [21]. Therefore, EAFD is classified as hazardous waste by the European Waste Catalog, the United States Environmental Protection Agency, and the NSW Environmental Protection Authority in Australia [22, 20, 21]. The direct disposal of this material is not permitted in many countries, and the material needs to be inertized or stabilized to prevent environmental contamination with toxic compounds [20, 22].

Grain size distribution

Fig. 3 shows the grain size distribution from a sieve analysis of an EAFD from a European steel producer. The D_{99} indicates that almost 90 % of the particles are smaller than 20

μm . The D_{50} diameter reveals that half of the EAFD consists of particles smaller than $1.3\ \mu\text{m}$.

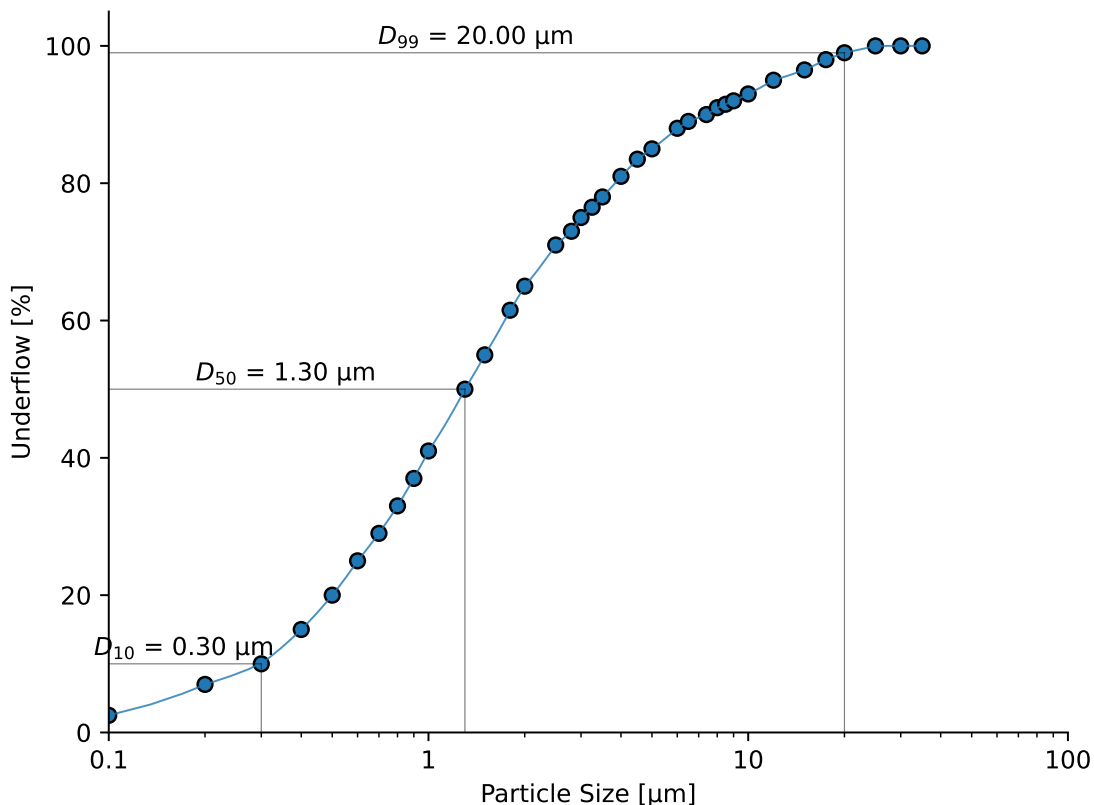


Fig. 3: Grain size distribution of EAFD

1.2 Recovery of electric arc furnace dust

Worldwide, zinc production slightly increased from 13 Mt in 2013 to around 13.5 Mt in 2022 [23]. 60 % of the produced zinc is used to galvanize steel to protect it from corrosion [23]. The main recycling route for scrap is the EAF, and all of the zinc in the scrap ends up in the EAFD, leading to a potential zinc recovery rate in the EAF of around 8.5 Mt to 13 Mt per year. According to the document for the nonferrous metals industries of the European Commission, the Best Available Technique (BAT) for the recovery of zinc from EAFD is the Waelz Process [24].

1.2.1 Waelz process

In the Waelz process, the zinc and iron oxides of the EAFD are reduced by carbon in a rotary kiln. The zinc oxide is reduced to zinc, which evaporates due to the high process temperature of around $1,200\ \text{°C}$. As it volatilizes into the counter-current gas flow, it re-oxidizes to small particles that leave the furnace together with the off-gas and can then be separated in bag house filters. In general, the Waelz process can be divided into three steps, as depicted in Fig. 4.

Material Delivery and Preparation

The material is delivered via trucks or trains and stored in silos if dry or in a warehouse if it contains moisture. To ensure a steady operation of the Waelz process, it is important

to mix the material to achieve a homogeneous feed material composition. Therefore, the carbon used as a reducing agent, the lime used to limit sintering, and the EAFD are mixed with some water and charged into the rotary kiln [25].

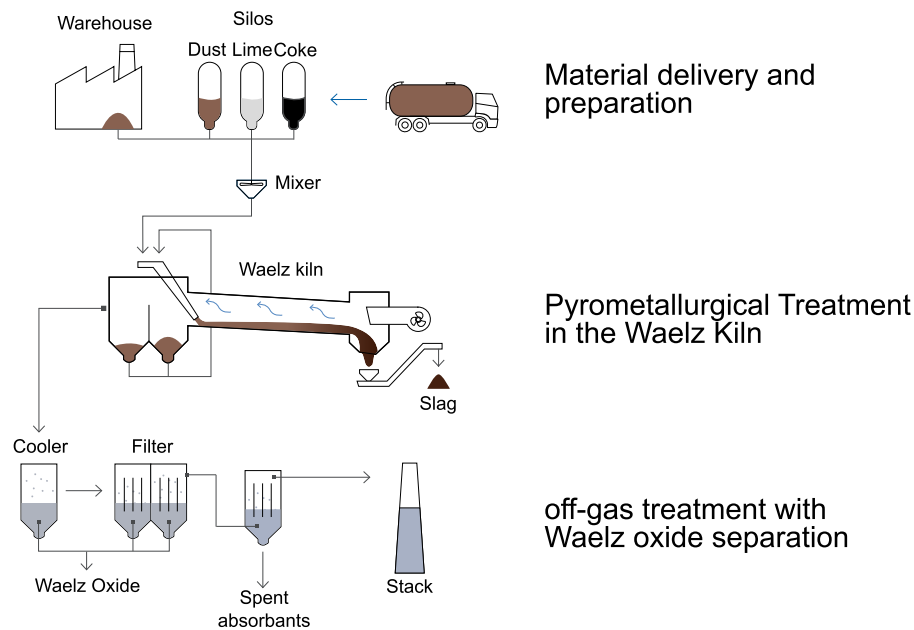
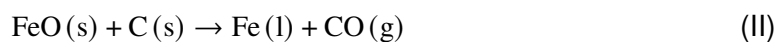
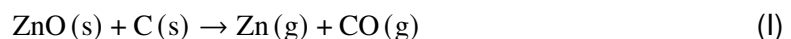


Fig. 4: Flow chart of the Waelz process [25]

Pyrometallurgical Treatment

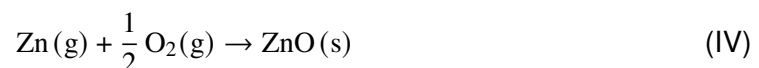
The solid feed enters the rotary kiln, which measures between 45 and 65 meters in length and has a diameter of approximately 3.5 to 4.5 meters. In the initial section of the kiln, the material undergoes drying and preheating from the hot gas flowing in a counter-current direction. Upon reaching a temperature between 1100 °C and 1200 °C, the oxides in the solid feed are reduced by carbon in an endothermic reaction, as seen in Eq. I and II.



The carbon also reacts with the oxygen present in the gas atmosphere to form CO_2 . According to the Boudouard equilibrium, the CO_2 further reacts with solid carbon to produce the reducing gas CO . Eq. III shows the Boudouard Equilibrium.



This CO gas then reduces the oxides in the feed. The rotation speed of the kiln, which ranges from 0.8 to 1.2 revolutions per minute, combined with factors such as kiln length, brick lining, and accretions, determines the residence time of the feed in the kiln, typically between 4 and 6 hours. During this period, around 90 to 95% of the zinc vaporizes and is removed by the counter-current flow, with subsequent re-oxidizing to zinc oxide upon contact with oxygen or CO_2 in the gas flow, as depicted in Eq IV.



The re-oxidation of zinc is exothermic and provides thermal energy for the endothermic reactions I and II. The reduced iron advances towards the kiln outlet, where additional air is introduced into the slag, leading to the exothermic re-oxidation of the iron.



The heat generated from this reaction is utilized to preheat the gas flow, thereby supplying the necessary thermal energy for the previously described endothermic reactions [25].

Off-Gas Treatment

After exiting the rotary kiln, the exhaust gas enters a settling chamber, where heavier particles, primarily carry-over from the feeding, are separated and recirculated back into the kiln. Additionally, the gas is cooled via water injection to reach the appropriate working temperature for the subsequent filtration stage. In the first filter stage, the dust, commonly referred to as Waelz oxide, is extracted from the gas flow and temporarily stored in silos. Subsequent treatment stages involve the removal of furans, dioxins, and volatile metals [25].

A major advantage of the Waelz process compared to other pyro- or hydrometallurgical processes is that the process is heated by partial combustion of the cheap coke that is used. The overall process efficiency is high, because the energy required for the reduction of the oxides is recovered by re-oxidation close to the reduction zone. This eliminates the need for an external energy source during operation. The process itself is well-optimized and relatively robust in terms of feed material [13].

On the downside, the Waelz process produces 700-800 kg/t residues and primarily focuses on the recovery of zinc, underutilizing other elements [13]. Additionally, the produced secondary-grade crude zinc oxide has a high carbon footprint of more than 2000 kg/t of contain zinc.

The idea is to replace carbon as a reducing agent by hydrogen, in order to lower the carbon footprint of the recovered zinc oxide. The next chapter will investigate the reaction kinetics of the EAFD reduction using hydrogen as a reducing agent.

2 Experimental Procedure

The objective of the present thesis is to investigate the reduction behavior of EAFD when reacting with the reducing agent H_2 in the TGA. The experiments were conducted under varying temperatures and H_2O/H_2 ratios to investigate parameters that correlate with industrial processes. The TGA allows for studying the kinetics of the gas-solid reactions that occur during EAFD recycling. The coupling of the TGA with an MS gives detailed information about the actual gas composition within the furnace chamber. In addition to the reduction kinetics, the shrinkage behavior was investigated in a Digital Microscope DIMI in order to get more data that may help in understanding the fundamentals and limitations of the solid-gas reduction of Electric Arc Furnance Dust EAFD. The H_2O/H_2 ratio was adjusted from 0.0, representing a reactive gas flow consisting entirely of 100 % H_2 , to 1.2, corresponding to a reactive gas flow containing 40 % H_2 and 60 % H_2O .

2.1 Setup and data preparation

Overall, a series of 32 experiments was conducted. Tab. 2 outlines the parameters that were used during the experimental campaign to study the reaction kinetics of EAFD reduction. The temperature was varied within a range from 900 °C to 1,200 °C, which is the typical bulk temperature of the reduction zone in Waelz kilns.

°N	Trial	T °C	H_2O/H_2 -	Geometry	°N	Trial	T °C	H_2O/H_2 -	Geometry
1	V23	900	0.00	✗	17	V38	1100	1.00	✗
2	V39	900	1.00	✗	18	V4	1100	0.00	✓
3	V32	900	0.10	✗	19	V10	1100	0.20	✓
4	V27	950	0.40	✓	20	V8	1100	0.10	✓
5	V22	950	0.20	✓	21	V25	1100	0.00	✗
6	V7	950	0.10	✓	22	V21	1150	0.00	✓
7	V12	950	0.00	✓	23	V29	1150	0.40	✓
8	V30	1000	0.40	✓	24	V34	1150	1.20	✓
9	V36	1000	1.00	✓	25	V15	1150	0.10	✓
10	V42	1000	0.60	✓	26	V14	1150	0.00	✓
11	V13	1000	0.10	✓	27	V40	1150	0.60	✓
12	V6	1000	0.00	✓	28	V19	1170	0.00	✓
13	V28	1050	0.40	✓	29	V31	1200	0.40	✓
14	V5	1050	0.00	✓	30	V16	1200	0.00	✗
15	V41	1050	0.60	✓	31	V33	1200	0.70	✓
16	V37	1050	1.00	✓	32	V26	1200	0.10	✓

Tab. 2: Variation of process parameters across 32 experimental runs

The 'Geometry' column indicates whether it was possible to measure the geometry of

the specimens both before and after the experiments. Notably, at 900 °C, no geometry measurements are available, as the material was too unstable after reduction due to disintegration from zinc oxide fuming, iron oxide reduction and insufficient sintering.

2.1.1 Sample preparation

Before conducting the TGA reduction experiments, EAFD was pressed into cylindrical specimens. To prepare the cylindrical specimens, a powder compaction process was employed using a press with an electric cylinder. The following steps were performed:

- **Preparation of the Mold:** A cylindrical die with a fixed diameter of 7.5 mm was used to shape the specimens. The die consists of a die cavity and a punch. The die cavity defines the shape and size of the specimen, while the punch applies the pressure to compact the dust.
- **Loading the Powder:** The loose EAFD was carefully loaded into the die cavity. The amount of dust was adjusted in a way, so that the height of the resulting cylinder was roughly half of its diameter. In this manner, the maximum diffusion length of the sample is 3.75 mm.
- **Compaction Process:** The loaded die was placed in the press. The upper punch was then lowered into the die cavity, and a press force of 1000 N was applied using the electric cylinder and a weight cell coupled with an Arduino to ensure uniform compaction of the dust.
- **Ejection of the Specimen:** After the compaction process was complete, the pressure was released, and the compacted cylindrical specimen was ejected from the die cavity.

Fig. 5 shows a cylindrical dust sample after being compacting with the press system. EAFD contains several highly volatile substances, such as chloride and lead (compare with Tab. 1 of the Section 1.1.2). During the high-temperature treatment in TGA, these substances volatilize, resulting in a mass loss that does not correspond to the reduction reactions of zinc and iron oxides. In order to mitigate this, the volatile components were removed prior to the reduction tests, so that the weight change of the samples during the TGA treatment correlated mainly to iron and zinc oxide reduction. The volatile components were removed by clinkering the specimens in a muffle furnace at 1.000 °C for a duration of 24 hours. The mass loss of the samples in the muffle furnace was determined by measuring the masses before and after the treatment. The mean mass loss in the muffle furnace was determined to be 45 mg which was around 11 % of the initial mass, indicating the successful removal of lead and chloride. This pre-treatment process also enhances the mechanical stability of the specimens and prevents disintegration during handling and further experimental procedures. Before the samples underwent the actual reduction tests, their geometry and weight were measured. After damaging several specimens while measuring their height and diameter with a caliper, the DIMI was employed to non-destructively measure the geometry. The weight was measured using a precision scale of type METTLER TOLEDO AG204 DeltaRange.

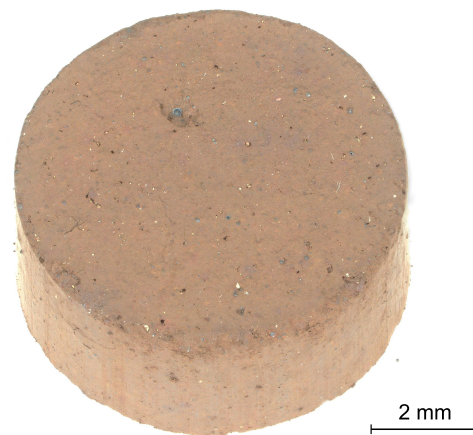


Fig. 5: Picture of a pressed EAFD specimen taken by the DIMI

2.1.2 Thermogravimetric analyzer

The used TGA in this experimental campaign is a Linseis STA PT1600 which allows to specify a temperature and gas profile. Fig. 6 illustrates the three segments of the setup configured in the Linseis software, marked by vertical dashed lines.

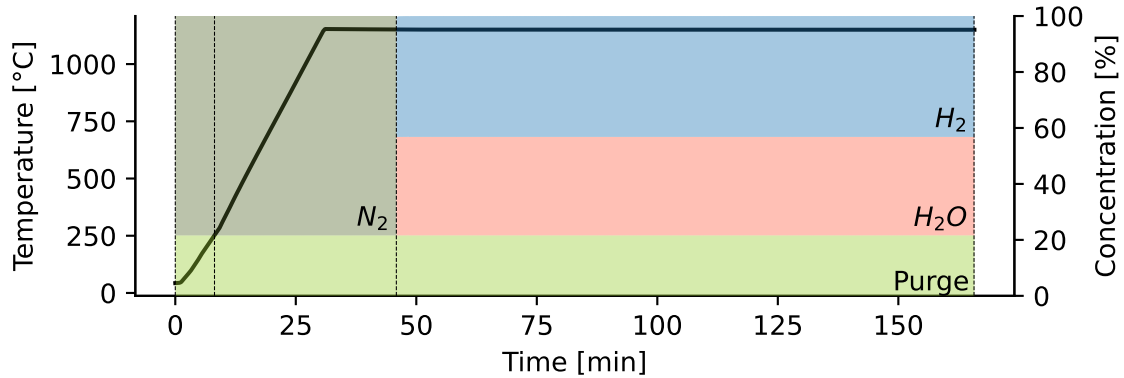


Fig. 6: Overview of the experimental setup in the Linseis software of the TGA

In the first segment, the furnace temperature is programmed to increase at a rate of 25 °C/min up to 250 °C. Subsequently, the heating rate is adjusted to 40 °C/min until reaching the target temperature specified in Tab. 2. After holding the temperature for 20 minutes to give the system time to reach a homogeneous temperature distribution, the third segment begins. The gas concentrations are visualized in form of area plots in the diagram. We used N_2 as the purge gas flowing through the weighing system. The N_2 concentration from the purge was maintained at 20 % of the overall gas atmosphere throughout all experiment. During heating and homogenization, the gas flow consists exclusively of N_2 . At the start of the reduction process, the part of the N_2 flowing through the reactive gas inlet is replaced by a gas mixture consisting of H_2O and H_2 with the depicted ratios outlined in Tab. 2. The duration of the reduction phase was set to 80 minutes.

When conducting the actual experiment with a EAFD sample in it, the concentration curve occurs quite different, as the whole system has an inertia, equivalent to the volume between the MFC and the MS. Therefore, the gradient of the MS concentration curve is not that steep. In Fig. 7 the lines show the H_2 concentration over the time after the switching from N_2 to 100 % H_2 . The dashed line is the concentration curve without the reduction of EAFD and represents just the mixing behavior of the gases in the reactor. On the other hand, the solid line shows the measured concentration by the MS, when an EAFD specimen is placed in to reaction chamber. The solid line deviates a lot from the dashed line, as the reduction of the oxides in the EAFD consumes H_2 . After configuring the parameters in the Linseis software, the EAFD specimen is placed inside a crucible on the sample holder within the reaction chamber. Fig. 8 illustrates the profile of the TGA. Once the system is closed and gas tight, the hydrogen

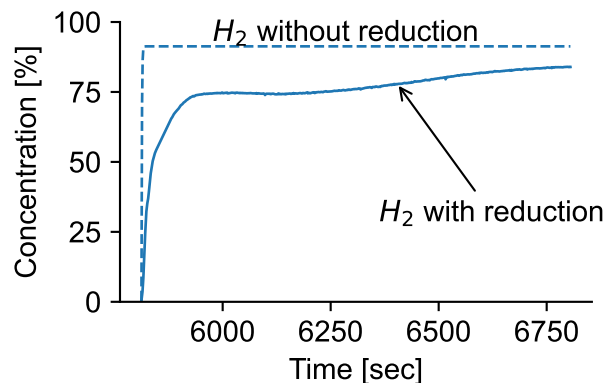


Fig. 7: Time dependent H_2 concentration with and without reaction

On the other hand, the solid line shows the measured concentration by the MS, when an EAFD specimen is placed in to reaction chamber. The solid line deviates a lot from the dashed line, as the reduction of the oxides in the EAFD consumes H_2 . After configuring the parameters in the Linseis software, the EAFD specimen is placed inside a crucible on the sample holder within the reaction chamber. Fig. 8 illustrates the profile of the TGA. Once the system is closed and gas tight, the hydrogen

safety box is activated, creating an overpressure of 0.15 bar in the system to prevent air infiltration, which could result in the formation of an explosive gas mixture. If any leakage occurs and the system pressure drops below the threshold of 0.1 bar, the safety box automatically terminates the experiment by flushing it with inert gas in order to prevent accidents.

The flow rates of H_2 , N_2 , and liquid water H_2O are controlled by Mass Flow Controller MFCs and mixed together and then enter the evaporator where the gas is heated up to 200 °C. Following the evaporation of H_2O , the gases pass through a heated pipe to prevent H_2O condensation, and enter the furnace at the gas inlet. Within the furnace, the gas reacts with the sample and exits the furnace chamber at the bottom flowing via pipes through a combustion flare to fully oxidize the exhaust gases. However, not all of the gas leaves the furnace via the bottom exit. A small fraction of these gases is directed through a quartz capillary towards the MS for the analysis of the exhaust gas composition. During reduction, gaseous zinc is formed that condenses in colder spots within the apparatus. To prevent condensation on critical components of the apparatus, a condenser with high thermal conductivity is installed in the furnace to have a controlled cold spot.

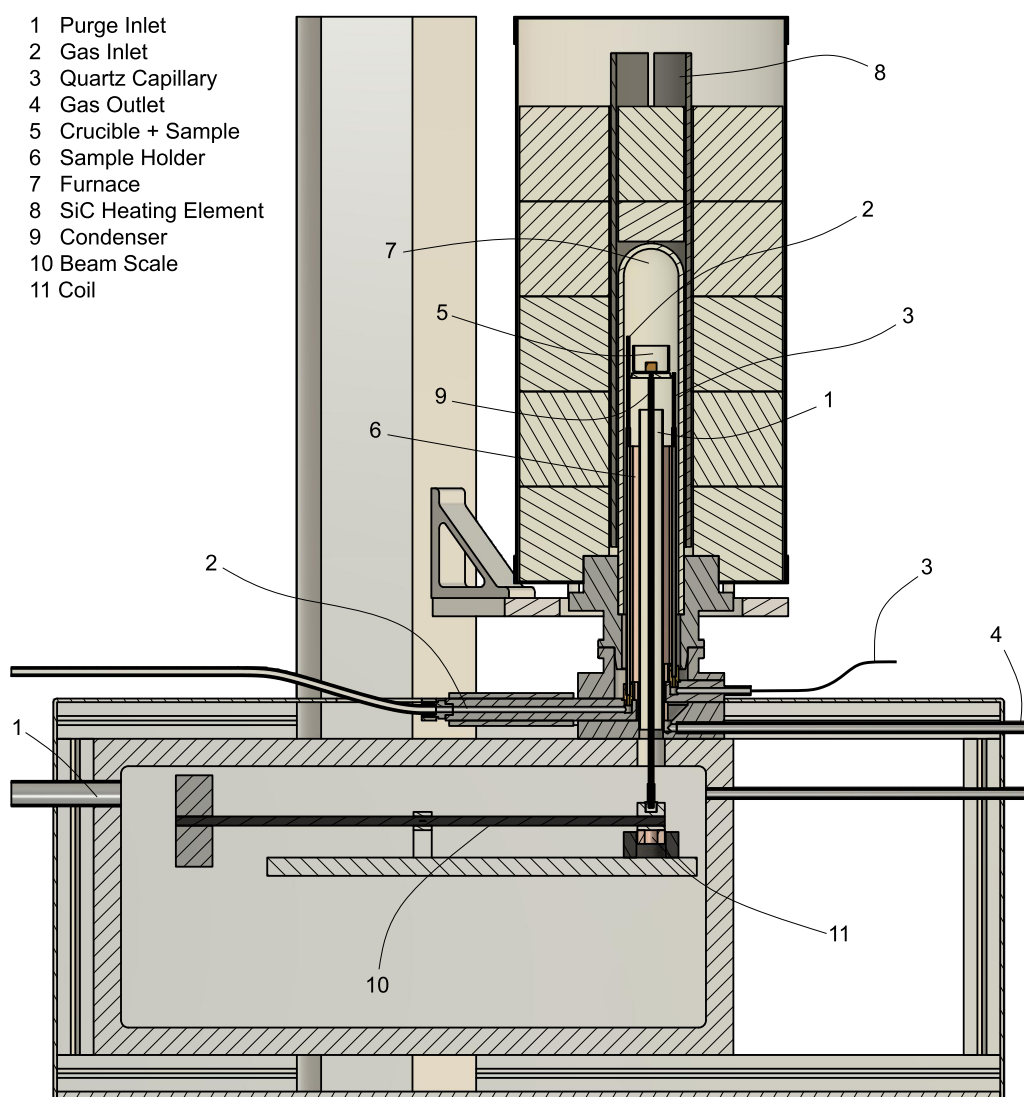


Fig. 8: Illustration of the TGA

During the reaction of the specimen with the reactive gases, its mass decreases because solid oxides are reduced and form H_2O . The sample holder is connected via a shaft

to one end of a beam scale that is located under the reaction chamber. This end of the beam scale is attached to a electric magnet that holds the beam in position by adjusting the electric current flowing through the coil. This current can be related to a mass change. A small fraction of the off-gas flows through the quartz capillary leading to the Mass Spectrometer MS of the type Pfeiffer ThermoStar GSD 350. The transfer line is heated to 200 °C to prevent condensation of H_2O and other gas species with a high condensation point. Within the MS, a vacuum pump maintains a working pressure of around 10^{-6} mbar. The molecules are ionized through electron bombardment and separated in the mass filter by their mass to charge ratio. Afterwards, the ion current is measured by a Faraday detector or a secondary electron multiplier and evaluated by the data analysis system. [26]

2.1.3 Data preparation

During the experiments all measured data from both, the MS and the TGA were sampled at a frequency of 10 Hz and stored in a FireBird database on the connected PC. For subsequent analysis, the experimental data was exported as csv-file, and underwent subsequent data preparation including cleaning, smoothing, and numerical manipulation.

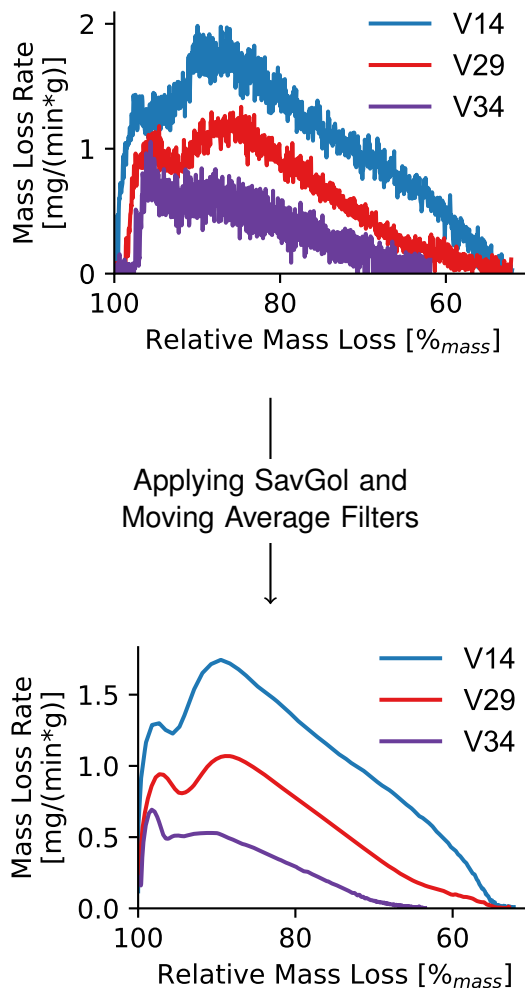


Fig. 9: Effect of applying a moving average filter and a SavGol filter to the raw data of the TGA

We prepared the initial data by applying a moving mean - and a Savitzky-Golay (SavGol) filter in order to smooth the over-sampled data from the TGA and MS.

The moving mean filter calculates the average of a specified number of data points within a distinct window that moves across the dataset by the number of data points after each calculation. Each calculation determines the mean value of a specific time-frame, effectively dampening short-term fluctuations and highlighting longer-term trends. This reduces the dataset length by the window length. [27]

To further refine data smoothness, a SavGol filter is applied. This filter fits successive subsets of adjacent data points with a low-degree polynomial through the least squares method. It minimally distorts the signal, while preserving critical data features such as relative maxima, minima, and their widths. [28]

This smoothing process is crucial, as variability in the raw data can significantly hinder data manipulation and visualization efforts. The top diagram of Fig. 9 illustrates the challenges presented by unfiltered data when attempting data manipulation with only limited smoothing especially when used for numerical deviation. The upper diagram exhibits high fluctuations, making

when used for numerical deviation. The upper diagram exhibits high fluctuations, making

it more difficult to see clear trends across the experiments. After applying both a moving mean filter and a SavGol filter, the numerical deviated data becomes smooth which improves the clarity of the data visualization substantially, as shown in the bottom diagram of Fig. 9.

The smoothed data allows for distinct identification of individual graphs without overlap, and clear trends can now be readily discerned. Once the data is smoothed, the manipulation phase of data preparation begins. The diagram on the top of Fig. 10 presents the raw data (relative mass m_{rel} over the time t) from the TGA for three different experiments. The data shows only the third experimental segment (description in Fig. 6), which represents the reduction segment. Notably, the gradients of the mass loss curves correlate directly to the reaction kinetics and vary significantly across the experiments, indicating variations in the different experiments.

Additionally, the extent of mass loss differs among the experiments, which may be attributed to variations in initial mass, fluctuating composition or to limiting reduction progress. To better analyze the reduction rate across these experiments, the mass loss rate dm_{loss} was calculated by numerically deviating the relative mass with respect to time. The calculated values are multiplied by -1 to calculate a positive value mass loss rate when the mass decreases. Additionally, these values were normalized with respect to the initial mass $m_{initial\ mass}$ of each experiment to facilitate comparison across different conditions, as shown in Equation 1. The diagram in the center of Fig. 10 displays the normalized mass loss rate over time. This visualization illustrates more clearly the reaction kinetics of the individual experiments, as the peak heights of the mass loss rates correlates directly with the reaction kinetics. However, plotting the reaction rate over time does not directly show the overall reaction progress of the sample. To include more characteristic information into visualization, we plot the mass loss rate versus the relative mass m_{rel} of the sample in the TGA.

The relative mass is calculated by dividing the absolute mass loss curve by the initial mass as outlined in equation 2. The next step involves inverting the x-axis to start at 100% of the specimen mass, thereby providing an intuitive representation of mass reduc-

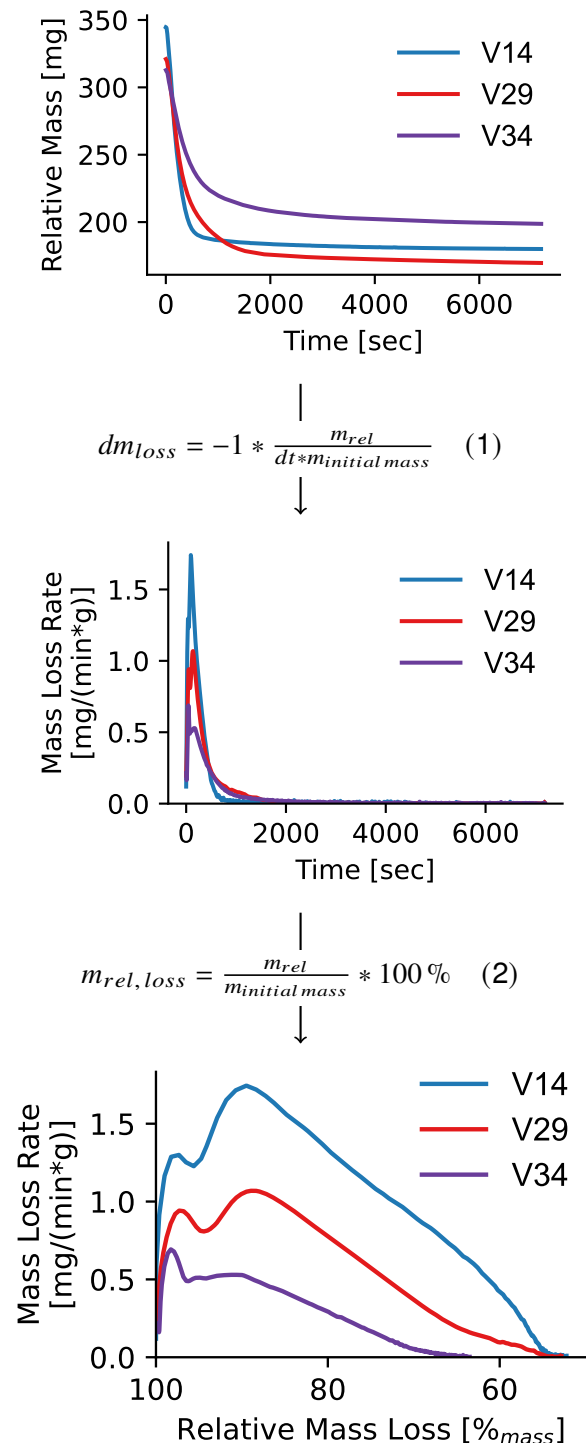


Fig. 10: Overview of data manipulation steps on the TGA data set

tion over time. The bottom diagram of Fig. 10 displays the normalized mass loss rate as a function of the relative mass of the specimen. This format offers a clear view of the reaction kinetics; a higher peak on the curve indicates a faster reaction at the corresponding stage of the reaction progress. Additionally, this illustration shows the reached reaction progress of the sample at the end of the experiment. These graphs are particularly useful to semi-quantitative compare experiments conducted at different process parameters, in the present thesis especially different H_2O/H_2 ratios and temperatures. In this way we are able to highlight the impact of these variables on the reaction kinetics.

2.2 Process parameter study

The process parameters in a pyrometallurgical treatment device influence the reaction kinetics of the reducible compounds as well as the achievable recovery and metallization rates. Therefore, having a comprehensive understanding of the influence of different parameters on the process is important. Using the TGA, we can investigate the following parameters: the sintering behavior, the shrinking of the material, the temperature, the gas atmosphere and the gas flow rate. This thesis investigates the influence of the temperature and H_2O/H_2 ratio on the reaction kinetics and the shrinkage behavior within an experimental campaign consisting of 37 independent reduction tests.

2.2.1 Reproducibility of the experiments

Reproducibility is a major requirement to ensure that experimental results are valid. To prove reproducibility, influencing factors such as the specimen mass, its geometry, or the gas flow rate were kept as consistent as possible and recorded and analyzed. Fig. 11 provides an overview of these parameters and their distribution.

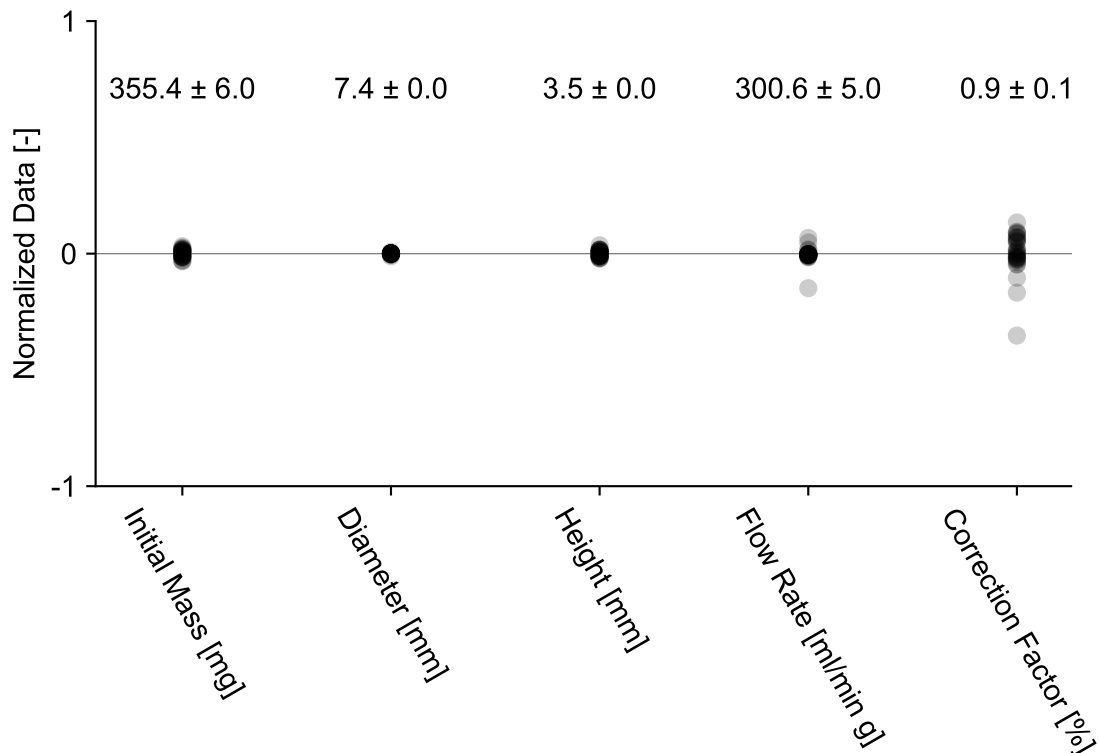


Fig. 11: Reproducibility of the experiments in the TGA

The values were normalized against their averages, and for each parameter, the mean

value and its standard deviation were calculated. This statistical analysis makes the experiments better comparable, ensuring that the results of the experiments are reliable and can be replicated under similar conditions. The target mass of EAFD for pressing specimens was 400 mg. After applying a defined force of 1,000 N to each cylinder to achieve a consistent geometry (diameter and height), which is critical to maintain a steady surface area. This consistency is vital because the reaction kinetics within the TGA are heavily influenced by the surface area and volume of the specimens. These factors affect how the tablets interact with gases during the reaction, directly impacting the results and reproducibility of the experiments.

The mass of the tablets was recorded at several stages: before pressing in the die, before clinkering in the muffle furnace, and before reduction in the TGA, as detailed in Fig. 12.

Initially, the mass of the unpressed powder was recorded with a mean of 401.6 mg and a standard deviation of ± 5.1 mg. After pressing, the average mass slightly decreased to 397.3 mg, while the standard deviation increased to ± 6.0 mg, indicating slight variations in the sample preparation process. The clinkering step (1000 °C for 24h) further reduced the mass to 355.4 mg with a standard deviation of ± 6.0 mg. The standard deviation of the specimens regarding their mass is 1.6% relative to the mean value (Fig. 12), indicating a high reproducibility of this experimental step and ensuring consistency in the conditions under which the reactions are conducted. All reduction experiments used a nominal gas flow rate of 300 ml/min per gram of sample. This overall gas flow rate consists of two components: the reactive gas flow of 240 ml/(min*g) and the inert gas flow of 60 ml/(min*g). To explore the effects of gaseous H_2O on reaction kinetics, the H_2O to H_2 ratio in the reactive gas flow was varied. Setting the gas flows at the MFC required the calculations outlined in Eq. 3 - 5. To calculate and set the H_2O flow rate ml_{liquid}/min in the MFC, the nominal reactive gas flow $\dot{V}_{reactive, nominal}$ was multiplied by the ratio $ratio_{H_2O/H_2}$. Since the result is in ml of vapor and the MFC settings are for liquid H_2O , the value had to be converted. The molar volume at standard conditions is 2241 ml/mol and the molar mass of water is 18 g/mol. To calculate the conversion factor, the molar volume was divided by the molar mass of water to get the volume of gas per gram. After converting the unit from ml/g to ml/ml by dividing it by 1 ml $H_2O/g H_2O$, the conversion factor is $1,240 \frac{ml_{vapor}}{ml_{liquid}}$, as detailed in Eq. 3.

$$\dot{V}_{H_2O, set} = \dot{V}_{reactive, nominal} * ratio_{H_2O/H_2} * m_{specimen} * \frac{1}{1240} \quad (3)$$

The nominal H_2 flow rate, $\dot{V}_{H_2, nominal}$, is calculated by subtracting the nominal gaseous H_2O flow rate $\dot{V}_{H_2O, nominal}$ from the overall nominal reactive flow $\dot{V}_{reactive, nominal}$. This result is then multiplied by the specimen mass to set the appropriate H_2 flow rate at the MFC as shown in the Eq. 4.

$$\dot{V}_{H_2, set} = (\dot{V}_{reactive, nominal} - \dot{V}_{H_2O, nominal}) * m_{specimen} \quad (4)$$

The set flow rate of the inert gas $\dot{V}_{inert, set}$ was also calculated by multiplying its nominal

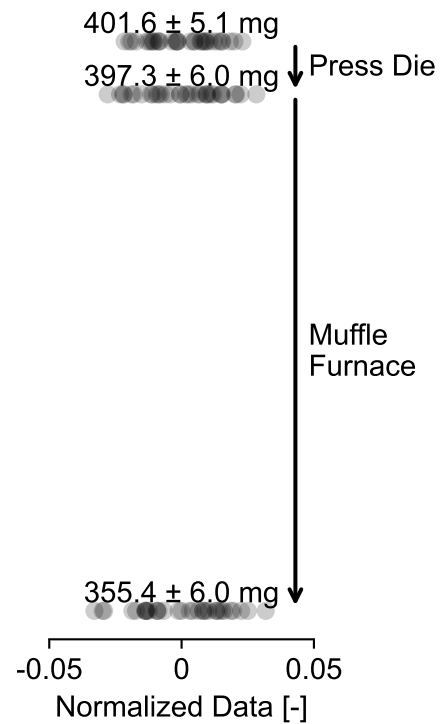


Fig. 12: Mass loss of the specimen during sample preparation

flow $\dot{V}_{inert,nominal}$ with the mass of the specimen.

$$\dot{V}_{inert, set} = \dot{V}_{inert, nominal} * m_{specimen} \quad (5)$$

The process of setting a nominal flow rate and normalizing it to the mass of each specimen placed in the furnace of the TGA was designed to enhance experimental reproducibility. This method compensates for mass variations among the specimens, ensuring a consistent ratio of reactive and inert gases interacting with each specimen. Fig. 11 shows the overall flow rates measured by the MFCs, which are then recalculated to determine the nominal flow rate of the gases. One value deviates notably from the mean, as depicted in the graphic. The outlier belongs to experiment V32 and there is no comment on what happened in the documentation of the experiments. However data from the MFC controlling the H_2O flow rate experienced high fluctuations and the signal of the MS detected a lower concentration of H_2O than was targeted via the H_2O/H_2 ratio. Therefore, we assumed that the water reservoir of the water pump was empty, which is why, this data point was not included into the calculations of the mean value and the standard deviation, although displayed in the graph itself. With these adjustments, the revised average flow rate was determined to be 300.6 ml/(min*g) with a standard deviation of ± 5.0 ml/(min*g). Another important step to improve the quality of experimental data is to calibrate the weight measurement from the beam scale in the TGA for each experiment. The integrated beam scale in the TGA is highly sensitive, but the position of the crucible and the sample on the holder influences the weight signal with a constant factor. These fluctuations can be eliminated with a correction factor that is derived by dividing the mass loss recorded by the TGA by the mass difference of the sample, measured with a precision scale (METTLER TOLEDO AG204 DeltaRange) before and after the reduction.

$$correction\ factor = \frac{\Delta m_{overall, TGA}}{m_{unreduced} - m_{reduced}} \quad (6)$$

A correction factor of 1 means that the beam scale measured the same mass change as the precision scale. However, the mean correction factor was approximately 0.9 (Fig. 11), indicating a systematic error in the beam scale. The standard deviation of the correction factors was found to be ± 0.1 , meaning a consistent linear correlation, which allows for reliably comparing results after applying the correction factor.

2.2.2 Experimental evaluation

The experimental evaluation mainly focuses on the analysis of reaction kinetics under varying process parameters. It additionally investigates the shrinkage behavior of the tablets during the reduction experiments in the TGA. The primary variable parameters were the H_2O/H_2 ratio in the reactive gas and the temperature. Of the 32 conducted experiments, some did not achieve the desired experimental quality, which will be discussed in the next section.

Influence of the different process parameters on the shrinkage behavior

We analyze the shrinkage behavior of the specimens using the digital microscope to measure the diameter and height of the cylinders before and after the reduction tests. Before reduction, the diameter of all samples was almost the same, with slight fluctuations in the height arising from different amounts of EAFD filled into the press die.

Temperature

Fig. 13 displays a comparison of the height and diameter of specimens before and after the reduction process. In the scatter plot, 'x' marks represent the geometry of the unre-

duced specimen prior to the experiment, while 'Δ' symbols indicate the geometry of the reduced tablets. Furthermore, the data points are color-coded based on the temperature at which the experiments were conducted. The lowest temperature was 950 °C, the highest temperature was 1.200 °C. It should be noted that, while experiments were also performed at a temperature of 900 °C, measurement of the geometry was not possible due to the disintegration of the sample during handling. This indicates that the specimens undergo insufficient sintering below 950 °C.

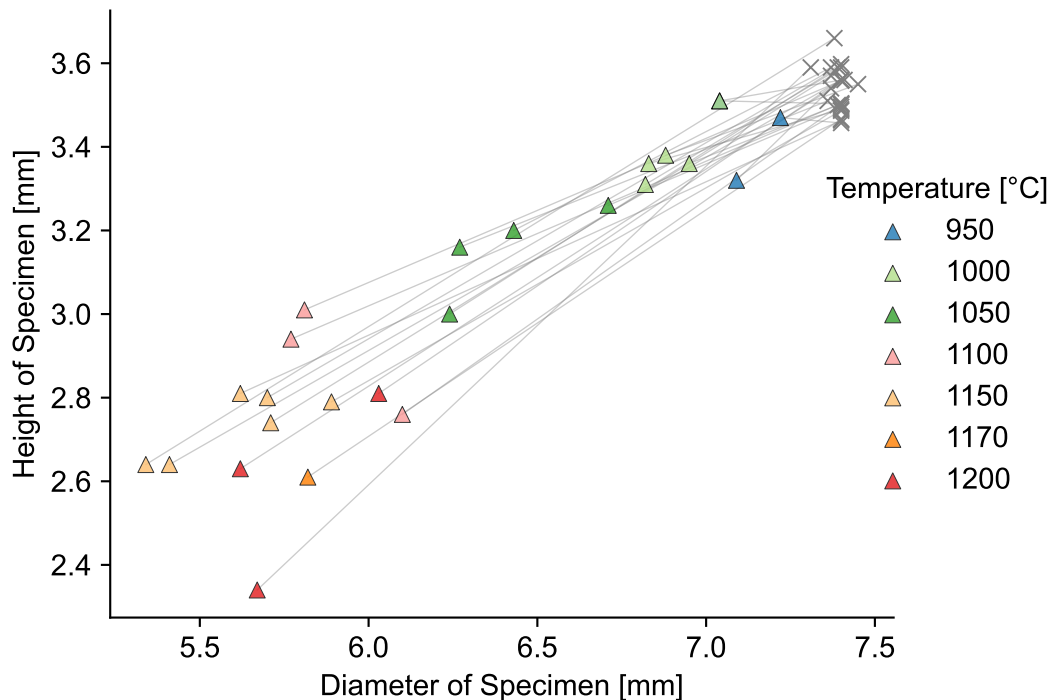


Fig. 13: Influence of the reduction temperature on the shrinkage behavior of the specimens

Experimental data shows a clear correlation between the shrinkage behavior and the reduction temperature. As the temperature of the reduction process increases, the specimens exhibit greater shrinkage. Additionally, gray lines in Fig. 13 connect the measurements of the specimens before and after the reduction experiments, illustrating a linear correlation between the extent of shrinkage and the increase in temperature. This derives from the similar gradients of the lines.

Fig. 14 displays several images of the EAFD tablets after reduction in the TGA for different temperatures. To ensure comparability, the scales of the images have been standardized to the same length. The single EAFD tablet at the top of the figure is an unreduced specimen after clinkering that serves as the reference. The specimens reduced at 900 °C were mechanically unstable and tended to break apart after removal from the crucible which is visible in the middle left image. In contrast, the other specimens were sufficiently sintered and maintained a stable geometry during handling. Higher temperature results in increased sintering which improves the mechanical strength of the sample. The volume loss increases with higher temperature but becomes steady above 1,100 °C. This is clearly visible in Fig. 14: the size decreases in the middle row from the left to the right but stays the same for the bottom row. This is also shown in the Δ scatter plot in Fig. 13. There is also a notable variation in the color of the specimens. At lower reduction temperatures the specimen are black, which transitions to a silver metal-like color with higher temperature. While this indicates a different metallization degree, the TGA reduction experiments detected the same overall mass loss. The sample reduced at 1,200 °C has

significantly visible macro pores. It seems that micropores transition to macropores when the temperature increases from 1,150 °C to 1,200 °C.

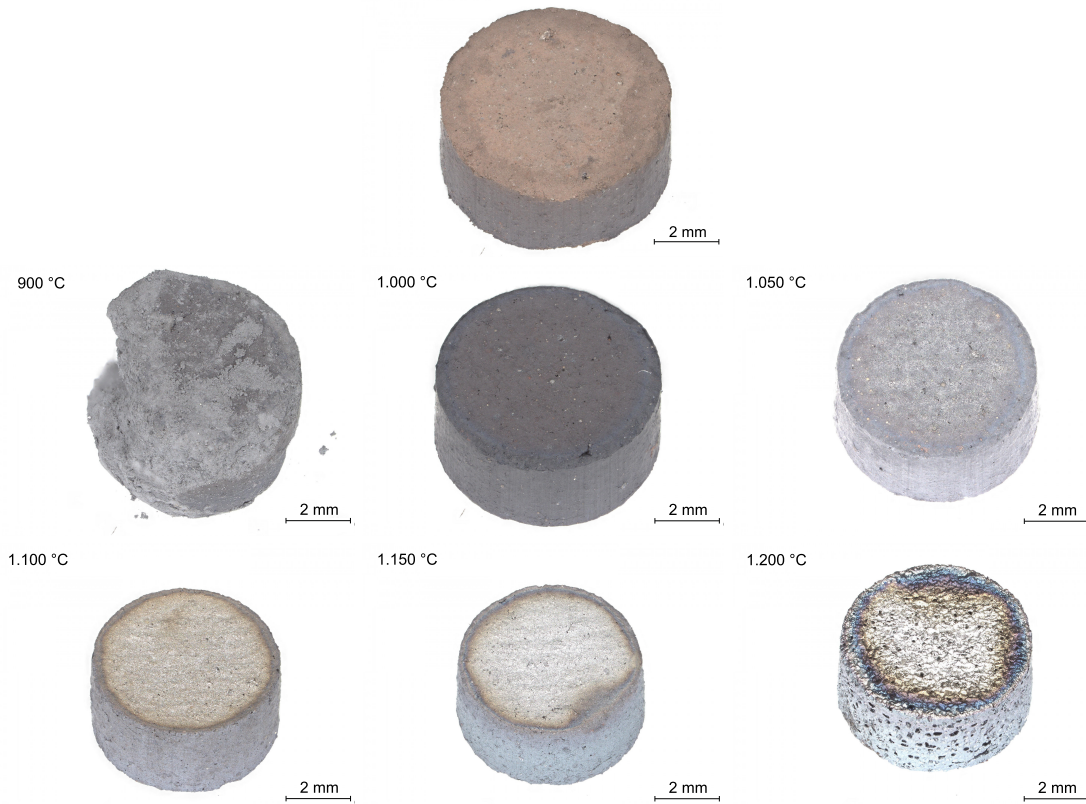


Fig. 14: DIMI pictures of the reduced EAFD specimen

We expected that the color-coded ' Δ ' symbols with the same color would be grouped more closely as found in Fig. 13. This high fluctuation suggested that shrinkage behavior depends not solely on the temperature, but also on the other variable, the H_2O to H_2 ratio in the reactive gas.

H_2O/H_2 - Ratio

After examining the influence of temperature on the shrinkage process, the focus shifted to comparing volume loss against temperature, as depicted in Fig. 15. Additionally, the data points are color-coded to estimate the impact of the H_2O/H_2 ratio in the reactive gas. For experiment V12, the sample broke before its geometry could be measured which is why the measured value is marked in form of an "x" in the plot. Throughout the experimental campaign, the H_2O/H_2 ratio was varied from 0.0 to 1.2. The color-coding in Fig. 15 transitions from bright colors for low H_2O/H_2 ratio to darker colors for higher H_2O/H_2 ratio. No geometric data was available for the experiments conducted at 900 °C, because of sample disintegration during handling.

Fig. 15 demonstrates that the shrinkage in the experiments increases with higher temperature. The shrinkage stagnates above a temperature of around 1,100 °C. However, it seems that H_2O/H_2 ratio also influences the shrinkage. At a constant temperature, the color coding suggests that lower H_2O levels decrease the shrinkage. However, the number of experiments conducted at varying H_2O levels is limited. For 1.170 °C there is only one data point limiting further analysis at this temperature setting.

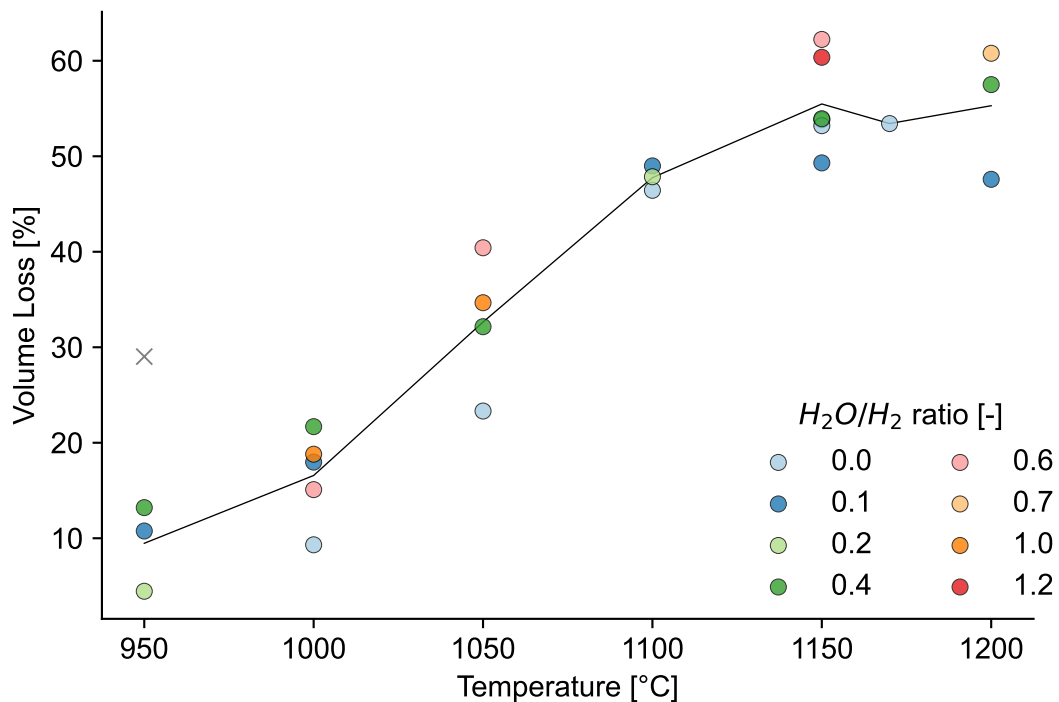


Fig. 15: Influence of the reduction temperature on the shrinkage behavior of the specimens

To better visualize the dependency of specimen shrinkage on the H_2O/H_2 ratio, the experiments were color-coded by temperature and plotted in a scatter diagram to compare the H_2O/H_2 ratio against the volume loss (Fig. 16). Linear regression was applied to the data groups (temperatures) to point out the trends with respect to the H_2O/H_2 ratio for different temperatures. Despite limited data availability — especially with the absent data at 900 °C and only one data point at 1,170 °C, and only three data points for 950 and 1,100 °C — the plot outlines a clear trend, showing a positive correlation between volume loss and the H_2O/H_2 ratio at which the reduction occurred.

Moreover, the graphs underscore that the volume loss is markedly affected by temperature. An exception is observed at 1,200 °C, where the slope is significantly steeper compared to other temperature-dependent graphs. At a H_2O/H_2 ratio of 0.1, the volume loss at 1,200 °C is similar or even lower than experiments conducted at 1,100 °C, 1,150 °C, or 1,170 °C. These data points may represent outliers, although two points are located at the same position, or it may indicate that specimen shrinkage is more sensitive at higher temperatures compared to lower ones. The different shrinkage behavior likely correlates with reaction kinetics, particularly the duration the sample contains lower-melting phases. The iron concentration of the investigated EAFD is 45 %, initially presented as hematite. During reduction, hematite transitions to magnetite and wustite before metallizing. Wustite melts at 1,377°C, magnetite at 1,597°C, hematite at 1,565°C, and metallic iron at 1,536 °C [29, 30, 31, 32]. Wustite also tends to form mixed phases, such as fayalite (melting point 1,205°C), which have even lower melting temperatures [33]. Consequently, we hypothesize that volume shrinkage increases with prolonged high wustite concentration at reduction temperatures, because the melting temperature correlates with the sintering temperature.

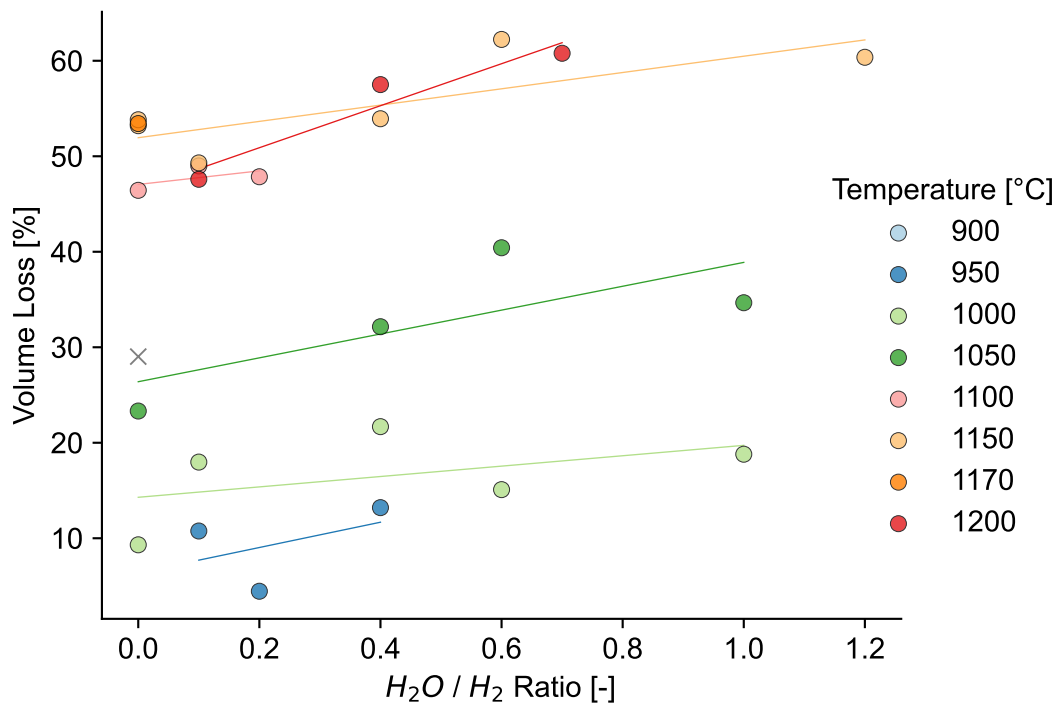


Fig. 16: Volume loss of the specimen influenced by the H_2O/H_2 - ratio of the reactive gas

The "x" scatter in Fig. 15 correlates to experiment V12 and indicates a broken sample before its geometry could be measured with the digital microscope.

Influence of the different process parameters on the reaction kinetics

In the next step, the influence of the H_2O/H_2 ratio and reaction temperature on the reaction kinetics was examined. Fig. 17 presents three highly different process parameters. The relative mass loss in percent is plotted on the x-axis and the normalized mass loss rate in $mg/(min \cdot g)$ is shown on the y-axis.

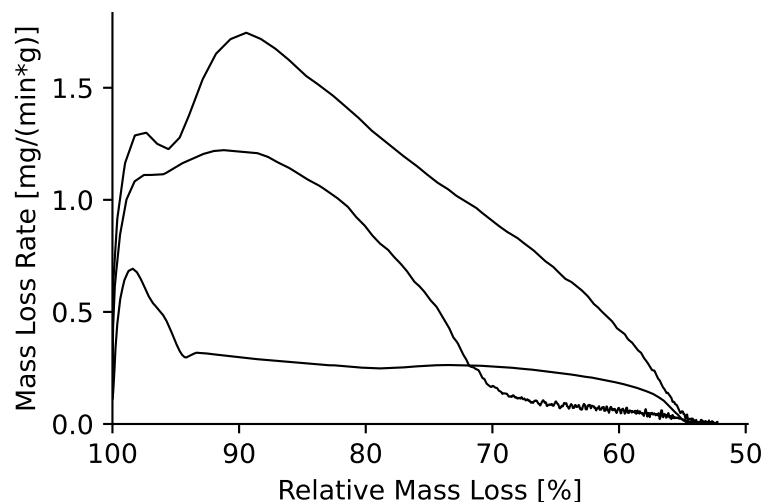


Fig. 17: Overview of reaction kinetics of experiments with different process parameters

The diagram outlines different kinetic profiles along the reduction progress; The mass loss rate curve of the experiment with the highest kinetic exhibits a local minima after a relative mass loss of around 5 %. The magnitude of the maximum mass loss rate

varies from 0.7 to 1.75 mg/(min*g). This variation highlights a dependency of the reaction kinetics on the reduction parameters, which is why we performed a detailed evaluation within the next sections.

Temperature

To analyze the influence of reduction temperature on the reaction kinetics, the same type of diagram as shown in Fig. 17 was plotted. The plots within this figure included experiments at different temperature with a constant H_2O/H_2 ratio to isolate the effect of temperature.

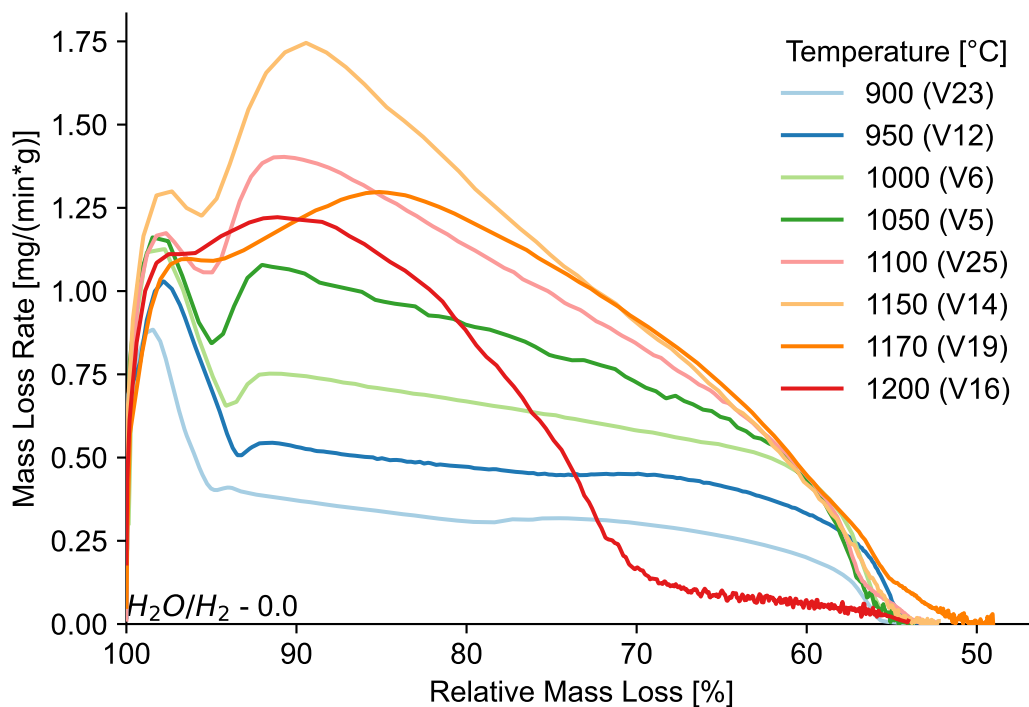


Fig. 18: Temperature dependent reaction kinetics at a H_2O/H_2 ratio of 0.0

Fig. 18 displays the temperature-dependent graphs of the reaction kinetics at an H_2O/H_2 ratio of 0. At this ratio, eight experiments have been conducted, ranging from 900 to 1,200 °C. The data proves a steep increase in reactivity with higher temperature up to 1,150 °C. At a temperature of 900 °C (light blue), the maximum mass loss rate was 0.9 mg/(min*g), whereas it was 1.2 mg/(min*g) at a temperature of 1,050 °C (dark green). This trend of an increasing mass loss rate at higher temperatures goes up to a temperature of 1,150 °C (yellow). Starting at 1,150 °C the reaction behavior during the reduction starts to change. The experiment at 1,170 °C show a lower reactivity for the first part of the reduction, but the highest reactivity in the second part. At 1,200 °C (red) the mass loss rate starts to drop off significantly within the first half of the reduction and had the lowest kinetics of all samples in the second part. That leads to the assumption, that the ideal maximum reduction temperature of the tested EAFD is between 1,150 °C and a maximum of 1,170 °C. It is important to emphasize that this behavior is only valid for isothermal reduction and may be different if the reduction occurs at constant heating, where a major part of iron oxide reduction to lower oxidation stages occurs at lower temperature.

Another observation is that the reaction kinetics are most intense during the initial phase of the experiment with a significant drop of after around 5% of mass loss for experiments performed below 1,050 °C.

All experiments have a local kinetic minima in this range, followed by a second maxima at around 90%. This second maxima is not prominent at lower temperature but becomes more significant up to 1,150 °C. Beyond 1,150 °C, the second peak shifts to the later reaction progress, while the first peak decreases in prominence. Tab. 3 summarizes the temperature influence on the peak prominence with respect to the local minima visible at a mass loss of around 5%. This table calculates and normalizes the prominence of the two peaks relative to their minimum between them. The calculation to make first and second rate maxima comparable was made with the following equation:

T °C	<i>Peak1_{diff}</i> %	<i>Peak2_{diff}</i> %
900	148.01	2.24
950	102.36	7.27
1000	71.54	14.92
1050	37.80	28.08
1100	10.90	32.70
1150	6.21	42.97
1170	0.55	19.27
1200	0.09	10.09

Tab. 3: Influence of the temperature on the different peaks of the reaction kinetic curve

$$Peak_{diff} = \frac{MassLossRate_{Peak} - MassLossRate_{Minima}}{MassLossRate_{Minima}} * 100\% \quad (7)$$

Furthermore, both peaks of experiment V19 conducted at a temperature of 1,170 °C are shifted towards a lower relative mass. Unfortunately, there was just one experiment conducted at that specific temperature, so it has to be confirmed if it is an outlier or if it takes such a different reaction path. Beyond 1,170 °C, the effect diminishes, but the second peak of the mass loss rate is still higher than the first. The first peak becomes smaller as the temperature increases from 1,000 to 1,050 °C. Those changes in the prominence of the two peaks have to be investigated in future research.

Fig. 19 shows the reaction kinetics dependent on the temperature at a H_2O/H_2 ratio of 0.1.

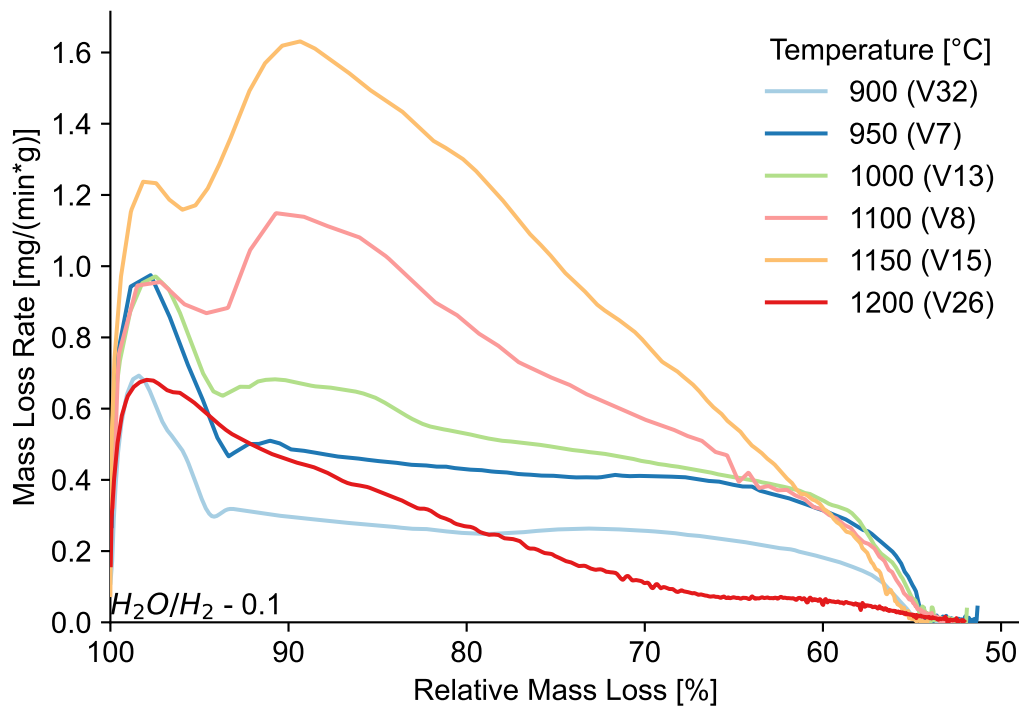


Fig. 19: Temperature dependent reaction kinetics at a H_2O/H_2 ratio of 0.1

The trend at a H_2O/H_2 ratio of 0.1 is similar to the experiments conducted in a H_2O/H_2 ratio

of 0.0. The mass loss rate in all experiments is significantly lower than those shown in the previous figure. The higher H_2O concentration lowers the reduction potential and simultaneously the lower H_2 concentration makes collisions between it and metal oxides less probable. Both factors together lower the reaction kinetics. Further investigations should evaluate the influence of each mechanism to better understand the overall reaction process.

H_2O/H_2 Ratio

The H_2O/H_2 ratio in the reactive gas is next to the furnace temperature a major factor influencing the reaction kinetics during EAFD reduction.

Fig. 20 illustrates the impact of the H_2O/H_2 ratio at a temperature of 1,000 °C. The kinetics and achievable reaction progress decrease as the H_2O/H_2 ratio in the reactive gas increases. In this figure, the experiment conducted with a H_2O/H_2 ratio of 1.0 ceases at approximately 65% of the initial mass, whereas experiments with a H_2O/H_2 ratio of 0.4 or lower continue until only about 55% of the initial mass remains. Furthermore, the second maxima of the mass loss rate gets less prominent with a rise in H_2O/H_2 ratio and fully disappears above a H_2O/H_2 ratio of 0.6. Tab. 3 provides a quantitative overview of the H_2O/H_2 ratio influence on the reduction kinetics at 1,000 °C.

H_2O/H_2	<i>Kinetics</i> mg/(min*g)	<i>Kinetics_{rel}</i> %
0.00	1.13	100.00
0.10	0.97	86.23
0.40	0.79	70.36
0.60	0.75	66.18
1.00	0.60	53.43

Tab. 4: Influence of the H_2O/H_2 ratio on the reaction kinetics

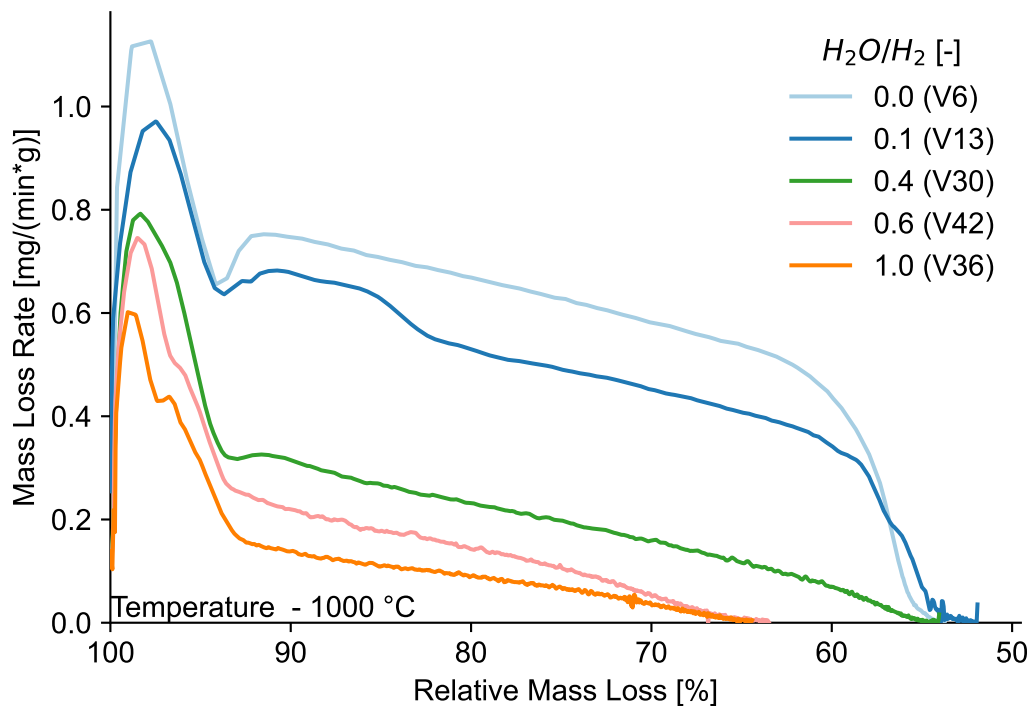


Fig. 20: H_2O/H_2 ratio dependent reaction kinetics at a temperature of 1,000 °C

The column labeled *Kinetics_{rel}* presents the maximum relative mass loss rate, expressed as a percentage of the maximum rate observed at a H_2O/H_2 ratio of 0.00. Notably, the

maximum rate decreases to around 50% when the H_2O/H_2 ratio reaches 1.00. Fig. 21 summarizes the determined kinetics of at 1,150 °C for H_2O/H_2 ratio of 0.0 to 1.2.

H_2O/H_2 -	Peak1 _{diff} %	Peak2 _{diff} %
0.00	6.21	42.81
0.10	6.72	40.65
0.40	16.98	32.84
0.60	23.45	23.45
1.20	42.92	5.34

Tab. 5: Influence of the H_2O/H_2 - ratio on the mass loss rate at 1,150 °C

At this temperature, second reaction maxima are visible for all experiments. The first maxima is higher than the second one for a H_2O/H_2 ratio up to 0.6. Above 0.6, the second maximum is higher. This indicates a strong influence of the H_2O/H_2 ratio on the second reaction maxima. The relative magnitude of the first peak is proportional to the H_2O/H_2 ratio. Tab. 5 demonstrates this dependency by comparing the local maxima as outlined in Eq. 7. The previous figures show the influence of the H_2O/H_2 ratio on the reaction kinetics of the EAFD. Those ratios were set by the MFCs, and does not

fully reflect the actual H_2O concentration of the atmosphere right next to the specimen in the TGA. That concentration should be a lot higher than the set concentration, due to the produced H_2O by the reduction of zinc - and iron oxide. The influence of the produced H_2O must be analyzed in further studies, by comparing the TGA data with the measured MS data.

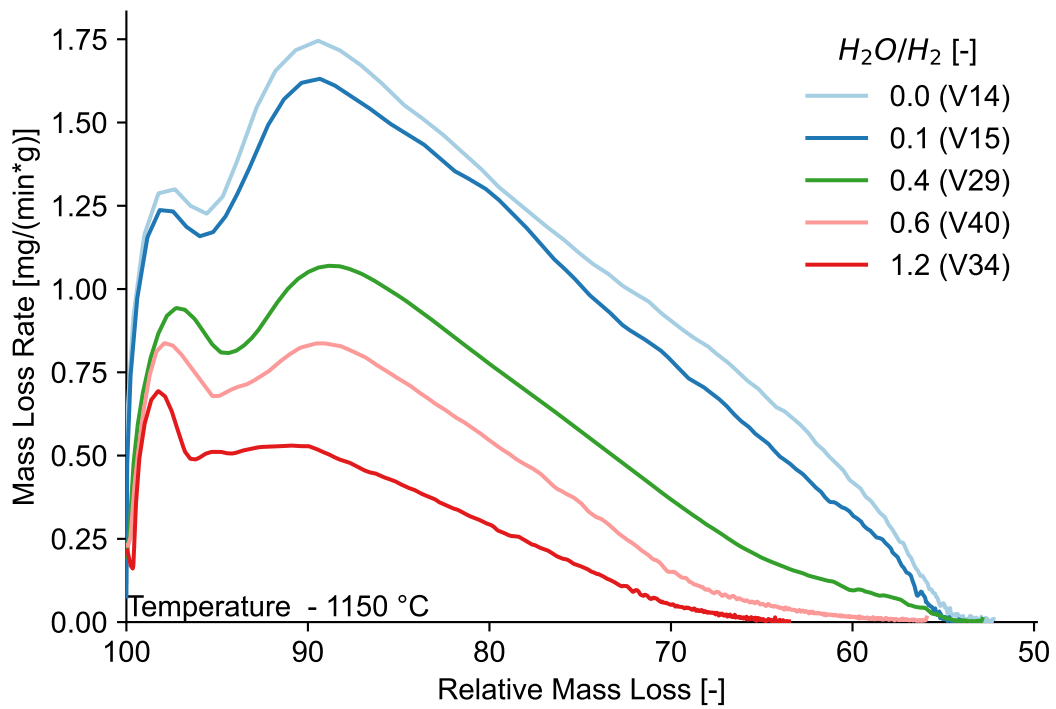


Fig. 21: H_2O/H_2 ratio dependent reaction kinetics at a temperature of 1,150 °C

2.3 Quantitative influence of process parameters on the reaction kinetics

In the previous chapter, the influence of varying process parameters on the overall reaction kinetics was studied. The second objective of my thesis is to investigate the reduction of zinc oxide in the EAFD. Therefore, it was necessary to separate the reduction of zinc oxide from the reduction of iron oxide. The TGA can only measure mass over time, which does not allow to distinguished between different reduction reactions. However, the coupled MS can be used to develop a new approach that can separate the iron oxide from the zinc oxide reduction.

2.3.1 Methodology

In the EAFD reduction experiments, we investigated the overall reaction kinetics in the TGA and analyzed the composition of the exhaust gases with MS. When hydrogen starts to flow, it reacts with the oxides in the EAFD, producing H_2O . Fig. 22 shows how the increase in water vapor concentration signals the onset of the reaction between hydrogen and the zinc - and iron oxide oxides. The MS data illustrates how the gas atmosphere of the furnace chamber acts as a buffer. This means that the actual hydrogen concentrations in the reaction zone deviate from the set values of the MFCs. While the MS provides data on gas concentrations, it lacks flow rate information, making it challenging to quantify the amount of H_2O produced or respectively, hydrogen consumed.

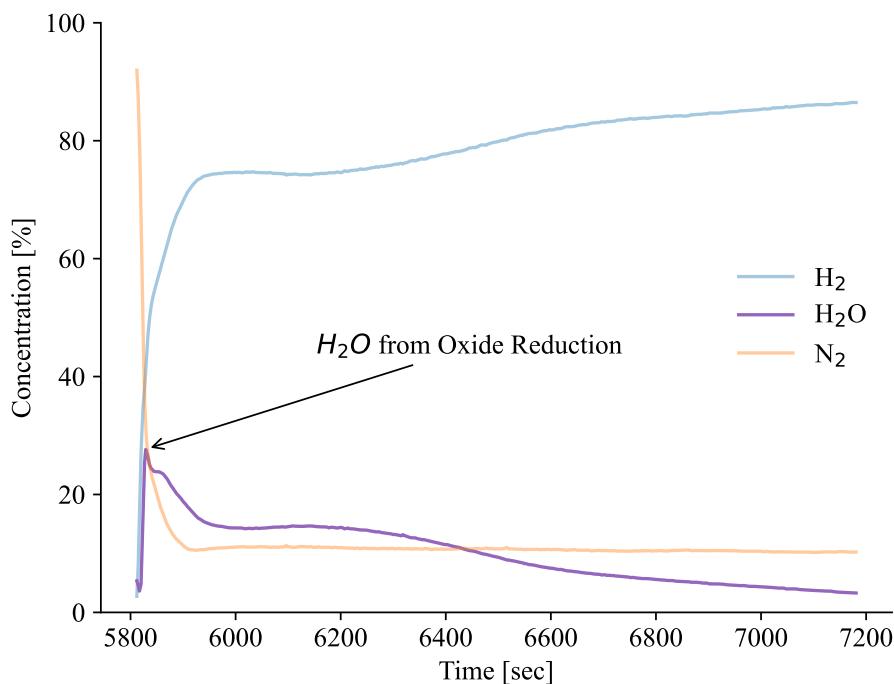


Fig. 22: Diagram of H_2O production measured by the MS

When oxygen or zinc and oxygen evaporate, the TGA measures a mass change. A numerical deviated form of the mass signal is illustrated in Fig. 23. The negative deviation correlates to a mass reduction and to some extent mirrors the shape of the H_2O concentration curve measured using the MS and shown in Fig. 22. Therefore, both signals to some extent correlate to the reaction kinetics. While the TGA is sensitive to the overall

mass loss (e.g. zinc and oxygen), the MS is sensitive to oxygen alone.

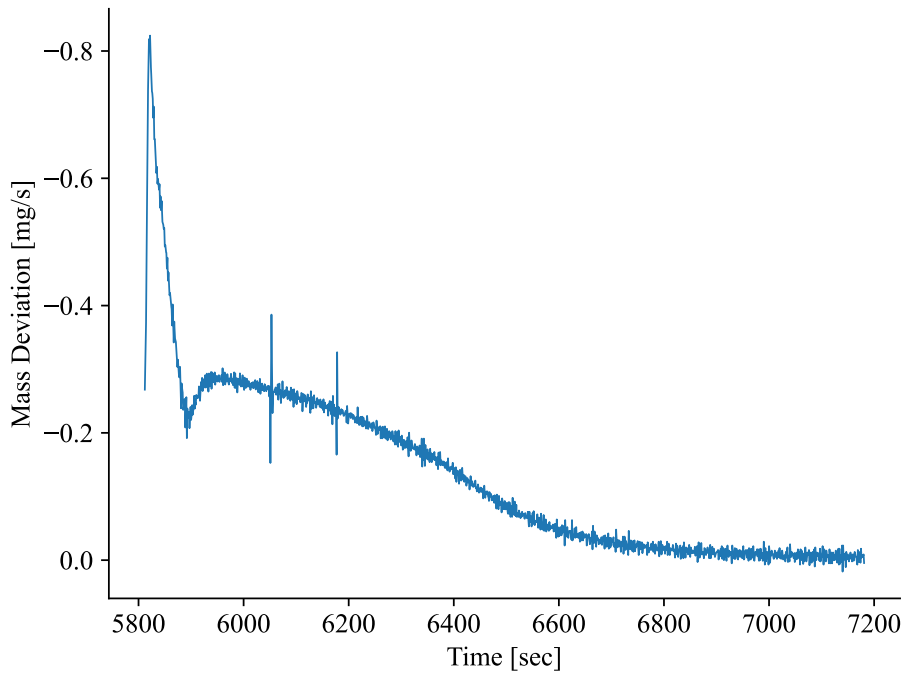
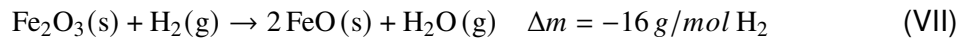


Fig. 23: Raw data of the mass deviation measured by the TGA



As zinc oxide reacts to gaseous zinc and H_2O , the mass loss measured by the TGA is 81 g for each mole of H_2O that is generated (compare Eq. VI). In contrast, if hydrogen reacts with other metal oxides (e.g. iron oxides), it forms only gaseous H_2O , meaning that the TGA measures only 16 g of mass loss for each mole of generated H_2O as the metal product remains on the scale of the TGA. As the EAFD specimens underwent a clinkering treatment, the main reactions are iron oxide and zinc oxide reduction. Therefore, the mass loss per mole of H_2 must be in range between 16 g and 81 g. To differentiate between the reduction of the two oxides, the main crucial step is to allow monitoring of the H_2 consumption and H_2O production rate over time. We can then calculate the mass conversion rate, by connecting the mass loss rate with the H_2 consumption rate (Eq. 8). In Eq. 8, \dot{n} is the consumption rate in moles per second (mol/s), MCR represents the mass conversion rate at the given time in grams per mole (g/mol), and \dot{m} relies to the mass loss rate in grams per second (g/s).

$$MCR = \frac{\dot{m}_{\text{TGA}}}{\dot{n}_{\text{H}_2, \text{consumed}}} \quad (8)$$

In this context, a mass conversion rate of 81 g/mol correlates to pure zinc oxide reduction to gaseous zinc and H_2O . On the other end, a mass conversion rate of 16 g/mol correlates to pure iron oxide reduction.

Calibration of the mass spectrometer

The calibration of the MS must be verified for the gases used in the experiments to get precise concentrations of the sensor for the exhaust gas coming from the reaction chamber. We assume, that the MFCs are calibrated correctly and that the actual values of the MFCs do not vary a lot from the set values.

However, the MFCs present a significant uncertainty as they are not regularly calibrated, which is a source of error. Additionally, the MS is calibrated using the MFCs from the TGA causing additional source and the calibration of the MS is performed for a single gas composition. The idea to overcome the limitation and possible errors from the single point calibration was to develop a multi-dimensional correction curve that accounts for various gas flow compositions from the MFCs. To generate data for this approach, a series of experimental runs was conducted, which were designed to provide a graphical representation of accuracy and correlation between the set values of the MFCs and the measured values from the MS. This method help to illustrate the reliability of the measurement system. The data generation for the correction curve involved setting the mass flow controllers for N_2 , H_2 , and H_2O to specific values, to establish gas atmospheres predefined in a calibration protocol. After setting the MFCs, the concentrations of N_2 , H_2 , and H_2O was measured until an equilibrium was reached. The measured equilibrium values were then compared with the set values to determine the measurement error. The calibration protocol consisted of 52 different gas configurations, to ensure a comprehensive coverage of various gas compositions and gas flow rates. The tests spanned a range from 0 to 100% for both H_2 and N_2 , and 0 to 31% for H_2O (, as outlined in)Tab. 6). The total flow rate for these tests is consistently maintained at 200 ml/min . The initial series of runs began with 0% H_2O , 60% H_2 and 40% N_2 . The concentration of N_2 was then gradually increased to 100%, while the H_2 concentration was decreased to 0%. Following this, the H_2O concentration was set at 0.01 ml/min or 6.20%, with corresponding adjustments in H_2 concentration to 84% to maintain the total flow rate. The minimal N_2 concentration remained at 10% as the purge gas flow (Compare with section 2.1.2) was fixed at 20 ml/min . This calibration sequence was repeated until the H_2O concentration reached 0.05 ml/min or 31.00%. This extensive calibration ensured that the mass spectrometer can accurately measure these gases under a variety of conditions, and provided reliable data for further analysis. During this calibration runs, the H_2O concentration could not exceed 31% because steam condensation clogged the quartz capillary due to a cold spot (further details are examined in section 2.3.1). The results of the the 52 configuration runs were examined using a graphical approach (Fig. 24).

H_2O (ml/min)	H_2O (%)	H_2 (%)	N_2 -Purge (%)	N_2 (%)
0.00	0.00	90.00	10.00	0.00
0.00	0.00	80.00	10.00	10.00
⋮	⋮	⋮	⋮	⋮
0.00	0.00	0.00	10.00	90.00
0.01	6.20	84.00	10.00	0.00
⋮	⋮	⋮	⋮	⋮
0.02	12.40	77.50	10.00	0.00
⋮	⋮	⋮	⋮	⋮
0.03	18.60	71.50	10.00	0.00
⋮	⋮	⋮	⋮	⋮
0.04	24.80	65.00	10.00	0.00
⋮	⋮	⋮	⋮	⋮
0.05	31.00	59.00	10.00	0.00
⋮	⋮	⋮	⋮	⋮
0.05	31.00	0.00	10.00	59.00

Tab. 6: Concentration set by the MFCs in order to determine a calibration curve for MS

After setting the MFCs, the concentrations of N_2 , H_2 , and H_2O was measured until an equilibrium was reached. The measured equilibrium values were then compared with the set values to determine the measurement error. The calibration protocol consisted of 52 different gas configurations, to ensure a comprehensive coverage of various gas compositions and gas flow rates. The tests spanned a range from 0 to 100% for both H_2 and N_2 , and 0 to 31% for H_2O (, as outlined in)Tab. 6). The total flow rate for these tests is consistently maintained at 200 ml/min . The initial series of runs began with 0% H_2O , 60% H_2 and 40% N_2 . The concentration of N_2 was then gradually increased to 100%, while the H_2 concentration was decreased to 0%. Following this, the H_2O concentration was set at 0.01 ml/min or 6.20%, with corresponding adjustments in H_2 concentration to 84% to maintain the total flow rate. The minimal N_2 concentration remained at 10% as the purge gas flow (Compare with section 2.1.2) was fixed at 20 ml/min . This calibration sequence was repeated until the H_2O concentration reached 0.05 ml/min or 31.00%. This extensive calibration ensured that the mass spectrometer can accurately measure these gases under a variety of conditions, and provided reliable data for further analysis. During this calibration runs, the H_2O concentration could not exceed 31% because steam condensation clogged the quartz capillary due to a cold spot (further details are examined in section 2.3.1). The results of the the 52 configuration runs were examined using a graphical approach (Fig. 24).

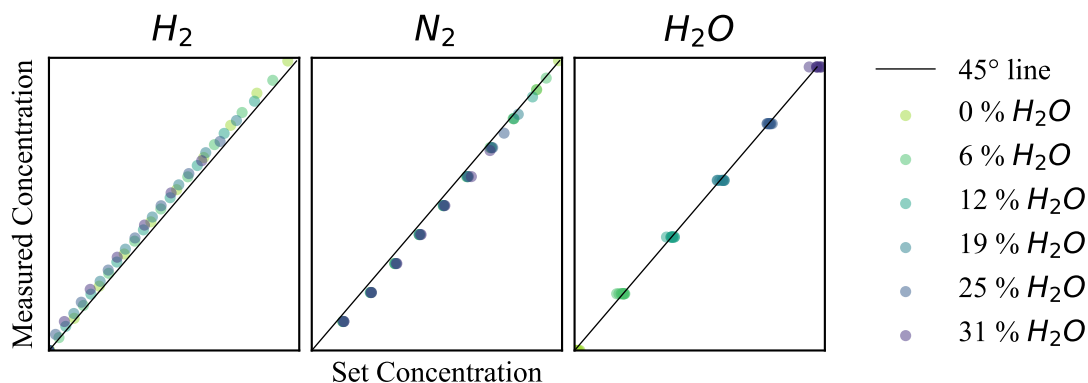


Fig. 24: Calibration curves of the MS for H_2 , H_2O and N_2

Three different plots were drawn, each incorporating a 45° line to serve as a reference. The x-axis of these plots represents the concentrations that should theoretically be set by the MFCs, while the y-axis displays the concentrations measured by the MS. Each data pair on a plot corresponds to one measurement. Data points lying on the 45° line correlate to no deviation between set and measured values. The greater the distance of a data points from this line, the larger the error for the corresponding gas atmosphere. The different N_2 and H_2 concentrations across six different levels of water vapor provide data to check if there is any systematic influence by either one of the gases. The plots for N_2 and H_2 in Fig. 24 demonstrate that the deviate between set and measured concentrations is small, and not affected by the vapor concentration in the gas flow. Remarkably, the curves show no complex influence from each other, indicating a good calibration of both, the MFCs and the MS. The slight offset from the 45° can be adjusted easily.

Steam condensation in the quartz capillary

During some experiments, peaks in H_2O concentration were observed where the measured value reached up to 100%, despite the set concentration being capped at 25% (Fig. 25). Initially, this discrepancy led to the assumption of a malfunctioning water pump, which was subsequently replaced. However, the problem persisted, ensuring that an alternative reason had to be found. It was hypothesized that the heat supply provided by the evaporator was insufficient to vaporize all the incoming water, causing the water level within the evaporator to rise, leading to a preheating of the liquid water in the evaporator. With the increase in the water level the surface area gets bigger compared to when water vaporizes directly at the inlet valve. This condition facilitates greater evaporation, leading to higher moisture content in the gas flow. Consequently, the gas reaches saturation, and even a slight drop in temperature results in the condensation of water in the quartz capillary, thus explaining the 100% water concentration readings observed by the MS. Despite disassembling the evaporator to check for malfunctions and even increasing the temperature settings, the issue continued, with the MS still recording peaks in water concentration. After the initial attempts to resolve the measurement problems were unsuccessful, another theory was proposed.

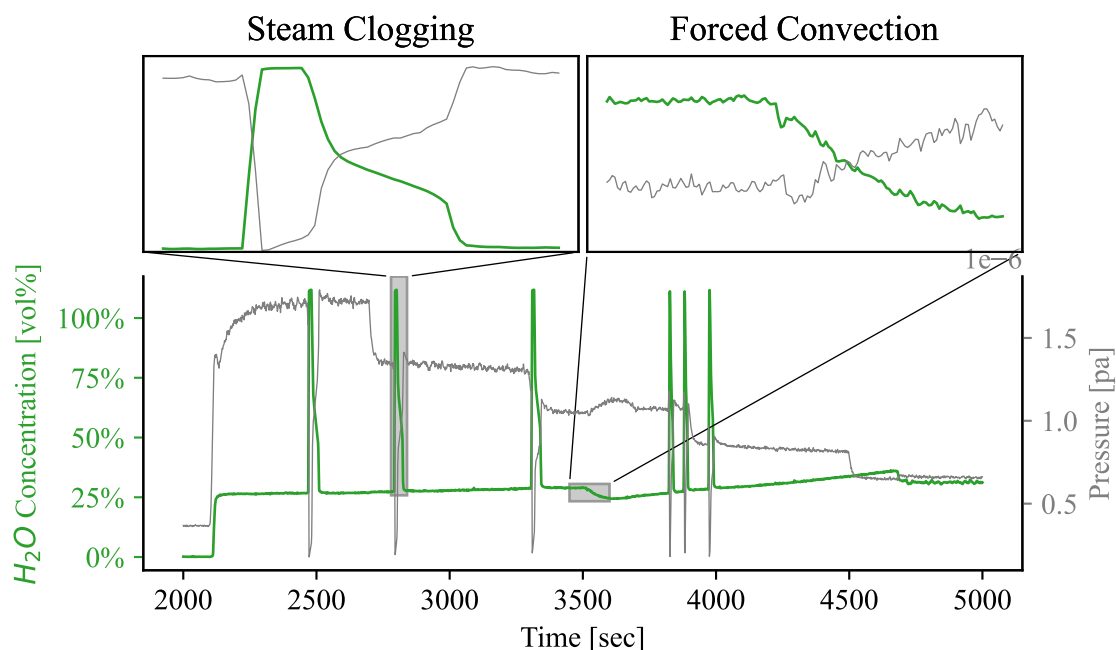


Fig. 25: Illustration of steam clogging in the quartz capillary

As explained in Chapter 2, all parts between the evaporator and the MS must be heated to prevent condensation within the system. Upon detailed investigation of the peaks in H_2O concentration, it was discovered that these peaks coincided with a rapid decrease in pressure within the MS as depicted in the diagram *Steam Clogging* in Fig. 25. This observation led to the hypothesis that a cold spot might exist within the system, causing vapor to condense somewhere in the transfer line between the furnace chamber and the MS. This condensation likely progresses to the point where the condensate begins to clog the quartz capillary. As the capillary becomes obstructed, the vacuum within the MS increases. However, the liquid water is believed to be slowly sucked through the capillary by the vacuum. Once the liquid leaves the cold spot, the pressure drops, because the water droplet in the quartz capillary evaporates. This causes the pressure to gradually increase until the droplet no longer obstructs the cross-section of the quartz capillary. This transition causes the MS to register a rapid increase in pressure and a decrease in H_2O concentration as other gases once again reach the detector. However, a higher concentration of H_2O is still detected because the quartz capillary still retains a thin layer of water from condensation in the cold spot. This continues until the residual water in the capillary fully evaporates, marking a point where both the H_2O concentration and the pressure return to normal levels. To identify the cold spot, a test run was conducted without a sample in the TGA, setting the H_2O concentration to approximately 25% (Fig. 25). While the experiment proceeded, the MS signal was continuously monitored on a nearby screen. After a period, the characteristic H_2O peaks reappeared. To pinpoint the location of the cold spot, an air pressure pistol was employed to target all potential areas within the system where a cold spot might exist. Concurrently, the H_2O signal from the MS was observed for any fluctuations in concentration. The forced convection caused by the air pressure pistol lead to increased heat flux between the inner surfaces of the targeted parts and the surrounding environment, enhancing heat dissipation and making steam more likely to condense. As the steam condensed, the vapor content in the remaining gas flow decreased, and the MS detected a reduction in H_2O concentration. When the

air pressure pistol was directed at the entry of the quartz capillary leading to the MS just after the lower flange of the furnace, a decrease in H_2O concentration was observed (illustrated in Fig. 25). This occurrence was unique to that specific point, confirming the hypothesis and identifying the location of the condensation. To prevent further condensation issues, a heat sleeve was installed around the affected component to maintain its temperature above the dew point of the steam in the gas flow. With this modification, the issue of steam condensation was effectively resolved, allowing for to perform experiments with high water vapor concentrations.

2.3.2 Gas model of the TGA reactor

The MS measures the concentration of the gas atmosphere (H_2O , H_2 and N_2), but cannot provide quantitative information about the gas flow rate or the consumption rate of H_2 .

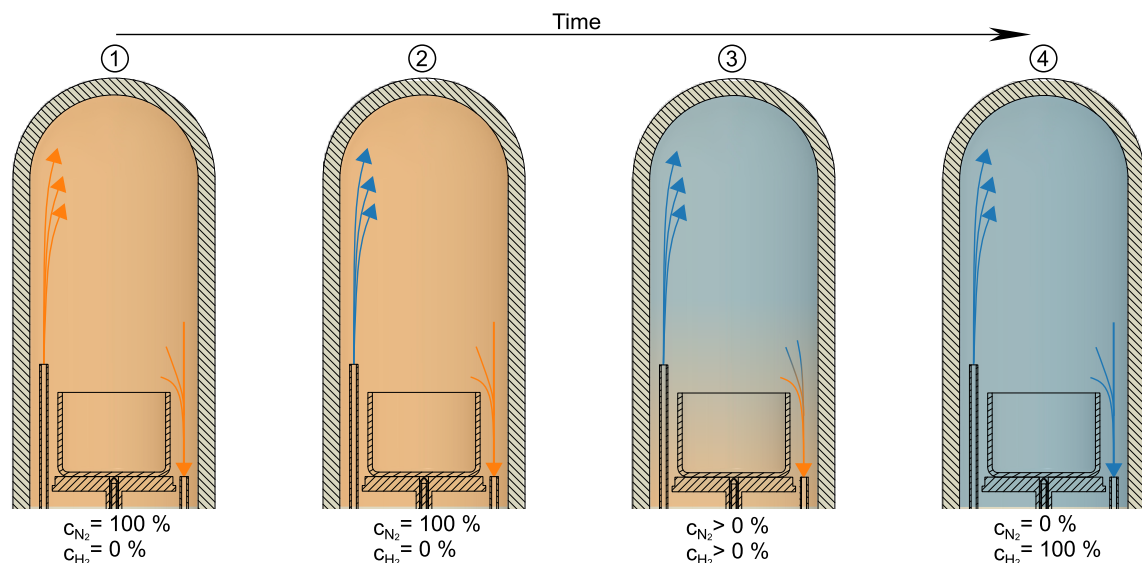


Fig. 26: Change in gas composition of the reactor when switching from N_2 (orange) to H_2 (blue) without EAFD specimen.

The idea is, to model the consumption rate combining the concentration from the MS and gas flow rate from the MFCs from the TGA and develop a model that describes the time-dependent change of the atmosphere as a function of inflowing gas flows. This model can then predict theoretical concentration for given flow rates of gases under non-reactive conditions. Using this model alongside experimental data, we can determine the flow rate-dependent volume of the model. In a first step, the model should simulate the mixing behavior of N_2 and H_2 gases. The stages are depicted in Fig. 26 as follows: (1) starting with pure N_2 , (2) switching the MFCs to pure H_2 , (3) mixing to a state with increasing H_2 , until (4) only H_2 remains, as detected by the MS.

The reactor model of the furnace chamber was developed assuming an ideal continuous stirred tank reactor. In such a reactor, the gas composition is constant over the whole volume without any concentration gradients. Consequently, the composition and temperature of the exhaust gas mirror the conditions within the reactor. The empty furnace includes no chemical reactions. Given a constant volume and pressure, the gas outflow equals the gas inflow. Fig. 27 outlines the locations of the points in the furnace used for the calculation. For the points 'Reactor pre' and 'Reactor post', the volume of the reactor is the same. The actual mathematical calculation was performed with the following variables:

In

flow rate $\dot{n}_{in, overall}$	[mol/sec]
temperature T_{in}	[°C]
concentration of element i $c_{i, in}$	[%mol]

Reactor pre

concentration of element i $c_{i, pre}$	[%mol]
volume reactor $V_{reactor}$	[l]
temperature reactor $T_{reactor}$	[°C]

Reactor post

concentration of element i $c_{i, post}$	[%mol]
volume reactor $V_{reactor}$	[l]
temperature reactor $T_{reactor}$	[°C]

Out

flow rate $\dot{n}_{out, overall}$	[mol/sec]
concentration of element i $c_{i, out}$	[%mol]

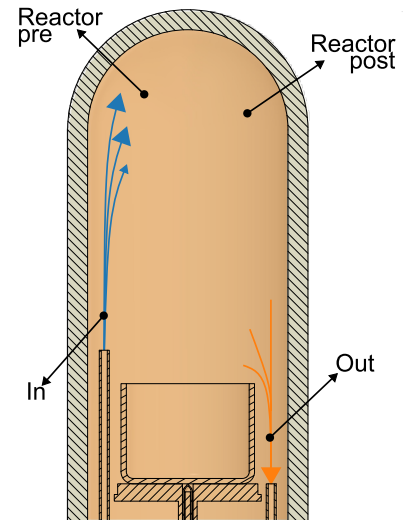


Fig. 27: Illustration of the functionality of the basic reactor model

To determine the volume of the reaction chamber model, we start with the initial experimental parameters. In this experiment, the gas flow switches from N_2 to H_2 . The hydrogen flow rate, \dot{V}_{H_2} , is specified in ml/min, and the initial gas concentration in the reactor is exclusively N_2 . We initially define the moles of gas entering at time t_0 by converting the inflow rate to moles per second, taking into account the molar mass of each component. This is mathematically expressed as:

$$\dot{n}_{i, in, t_0} = \frac{\dot{V}_{i, in, t_0}}{M_i} \quad (9)$$

This equation serves as the basis for further calculations in the reactor model, ensuring that all subsequent reactions and behaviors are based on accurate and consistent initial values. Given the high temperature and near atmospheric pressure (1.15 bar) within the reactor, we apply the ideal gas law to estimate both the virtual volume $V_{Reactor}$ and the moles $n_{i, Reactor}$ present:

$$p \cdot V_{Reactor} = n_{Reactor} \cdot R \cdot T_{Reactor} \quad (10a)$$

$$n_{Reactor} = \frac{p \cdot V_{Reactor}}{R \cdot T_{Reactor}} \quad (10b)$$

Using the ideal gas constant R defined as $8.314 \frac{Pa \cdot m^3}{mol \cdot K}$, we calculate the overall moles in the reactor via Eq. 10b and the component-specific moles through Eq. 11. Since the pressure and temperature within the reactor remain stable, the total number of moles does not vary over time. The formula to calculate the moles of each gas component in the reactor is given by:

$$n_{i, Reactor, t_0} = c_{i, Reactor, t_0} \cdot n_{Reactor} \quad (11)$$

To ensure consistency in calculations and reflect the unchanging conditions within the reactor, the total moles within the reaction chamber remain constant. This consistency requires that the moles entering the system must equal the moles exiting through the outlet pipe. For a given component i , the moles leaving the chamber at time t_0 are

calculated by multiplying the total incoming flow rate by the concentration of component i in the reactor at that time. The equation is:

$$\dot{n}_{i,out,t_0} = c_{i,Reactor,t_0} * \sum \dot{n}_{i,in,t_0} \quad (12)$$

Using the results from Eq. 9, 11, and 12, we can calculate the moles in the reaction chamber $\dot{n}_{i,Reactor,t_1}$ at timestamp t_1 . To achieve this, we subtract the outgoing moles \dot{n}_{i,out,t_0} from the sum of the incoming moles \dot{n}_{i,in,t_0} and the moles already present in the reactor, $\dot{n}_{i,Reactor,t_0}$:

$$\sum n = 0 \quad (13a)$$

$$\sum n_{ein} - \sum n_{aus} = 0 \quad (13b)$$

$$(\dot{n}_{i,in,t_0} + \dot{n}_{i,Reactor,t_0}) - (\dot{n}_{i,out,t_0} + \dot{n}_{i,Reactor,t_1}) = 0 \quad (13c)$$

$$\dot{n}_{i,Reactor,t_1} = \dot{n}_{i,in,t_0} + \dot{n}_{i,Reactor,t_0} - \dot{n}_{i,out,t_0} \quad (13d)$$

With Eq. 13d the concentrations of component i can be calculated as followed:

$$c_{i,Reactor,t_1} = \frac{\dot{n}_{i,Reactor,t_1}}{\sum \dot{n}_{i,Reactor,t_1}} \quad (14)$$

Using Eq. 14, we can proceed to the next iteration of calculations within our numerical model, which allows for the computation of time-dependent concentration changes for the gases in the reactor.

2.3.3 Results applying a single continuous stirred tank reactor

Eq. 10b shows the dependency of the modelled reactor volume for the calculation of the overall moles present in the reactor. The evaluation shows that the volume of the reactor model must be estimated for each individual flow rate of the entering gases.

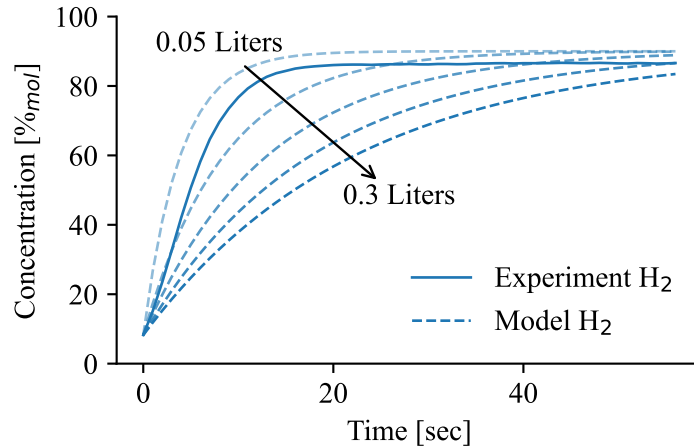


Fig. 28: Influence of the reactor volume $V_{Reactor}$ on the H_2 concentration curve of the reactor model

If this volume is underestimated, the model predicts that concentration changes occur more rapidly than they do in actual experiments. Conversely, if the volume is overestimated, the resulting concentration gradient is much smaller than that measured by the MS. Fig. 28 illustrates this phenomenon by comparing the experimental data of H_2 concentration over time observed by the MS against the predicted concentrations from the reactor model at various reactor volumes.

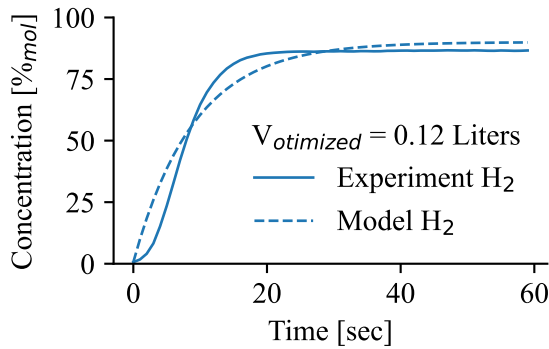


Fig. 29: H_2 concentration curve of the reactor model with the optimized volume $V_{\text{Reactor, optimized}}$

To determine the optimal volume for the reactor model, a least squares algorithm was implemented in Python. Initially, an initial reactor volume was set, with the least squares algorithm fitting an ideal value by iteratively adjusting the volume to minimize the deviation between the model predictions and the experimental data using gradient descent. Fig. 29 shows the experimental data measured by the MS compared to the predicted data calculated by the reactor model using the least square algorithm. This algorithm utilizes the numerical model describing the concentration curve as a function of the vol-

ume of the reactor and the gas inflow rate. The process begins with a given gas composition at $t=0$, and computes the concentration curve then over time. For each time step, the algorithm calculates the squared difference between the estimated and measured concentrations. This calculation is repeated for each observed/predicted value pair before the reactor's volume is slightly adjusted. If this adjustment results in a lower deviation from observed values, the algorithm uses gradient descent to adjust the volume of the model. This iterative process continues until a termination condition is met or after the algorithm performed a maximum number of iterations. Fig. 29 outlines significant discrepancies between the predicted and measured curves. Initially, the experimental data shows that the measured concentration curve from the MS is described inaccurately by the reactor model. It seems that the concentration change is caused by a mixture of two effects: diffusion and convection. Therefore, the simplified model needs refinements for a more accurate representation of empirical realities.

2.3.4 Results applying a series of continuous stirred tank reactors

To more accurately describe the observed effect curve, the reactor model was adjusted by setting up a series of CSTRs as some form of meshgrid (Fig. 30). It shows that more CSTRs in series results in a more flat concentration increase at the beginning of the process.

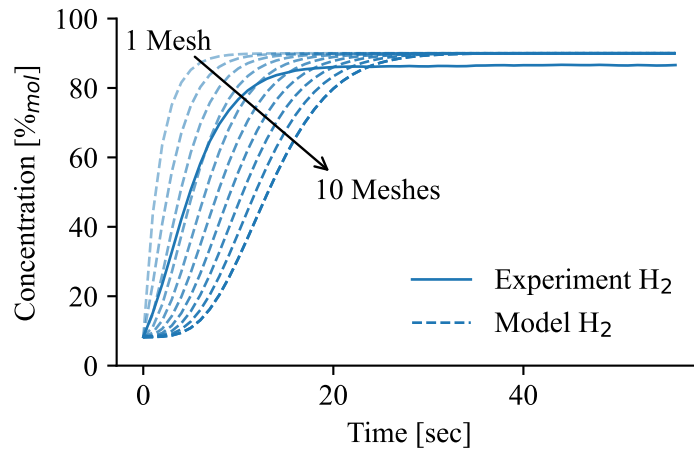


Fig. 30: Influence of the number of CSTRs on the inertia of the H_2 concentration of the reactor model

Fig. 31 schematically illustrates the implementation using two CSTRs within the reactor volume. The top panel of the figure shows the idea to describe the whole reactor with a single CSTR, as discussed in the previous chapter. The bottom panel shows the reactor divided into two CSTRs. In such a series of CSTRs, the inflowing gas reaches the upper segment of the reactor first. The computation within each segment mirrors that of the basic reactor model, with the difference that the output gas flow from one segment serves as the input for the subsequent segment. The time steps within the individual CSTRs is matched with the one from the experimental data.

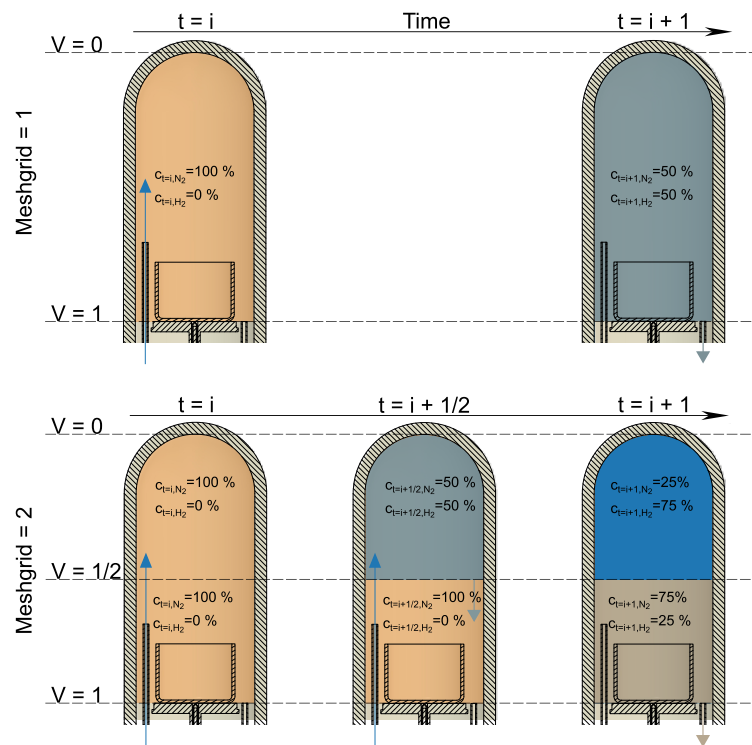


Fig. 31: Illustration of the implementation of CSTRs into the basic reactor model

The colors within the graphic visualizes the mixing of gases at specific time steps and

positions within the reactor where orange represents N_2 , and blue represents H_2 . The timeline begins at the left side with the time stamp $t = i$ and extends to $t = i + 1$. At the beginning of the calculation at $t = i$, the concentration is 100 % N_2 , with a inflow H_2 concentration of 100 % . Fig. 31 illustrates the effect of a flow rate corresponding to half of the reactor volume per time step. At the basic model of one CSTR, the volume of H_2 that enters the reactor in one timestep is half the volume of the reactor itself. Therefore, half of the reactors volume at $t=i$ is replaced by the inflowing H_2 gas. Consequently, at $t = i + 1$, the concentrations in the reactor model depicted in the top panel of Fig. 31 equalize to 50% N_2 and 50% H_2 . This is attributed to the ratio of the segment volume to the flow rate, which remains consistent with the single CSTR model, as both, the volume and the flow rate have been halved. For the second iteration $t = i + 1$, the gas in the top segment mixes again with the incoming gas flow, resulting in a gas composition of 75% H_2 and 25% N_2 . As the gas flow in the top segment displaces the same amount of gas with the composition of the previous iteration $t = i + 1/2$, the concentraion of the inflowing gas in the second segment is 50% H_2 and 50% N_2 resulting in a gas comprising 25% H_2 and 75% N_2 .

In this way, this model including two CSTRs in series delays the H_2 concentration increase of the outflowing gas in the early mixing phase. This illustrates that an increase in the number of mesh layers within the model leads to a decrease in H_2 concentration and an increase in inertia levels (Fig. 30). The number of CSTRs has to be an integer. As the least square algorithm to optimize the volume uses gradient descent it cannot be used applied on parameters that do not allow for small changes. Therefore, the ideal number of CSTRs was de-

termined manually. The ideal number was found to be 4 for as depicted in the scenario in Fig. 32. Following this modification, the modelled volume of the reactor was recalculated, revealing a decrease from the original 0.12 liters, (Fig. 29), to 0.03 liters per CSTR (Fig. 32) resulting in a reactor volume of 0.12 liters.

This theoretical reactor volume is calculated by the least square algorithm that changes it as long until the deviation between the model and the experimental data reaches a minimum.

2.3.5 The complex mixing behavior of the gas in the reactor

The reactor volume correlates directly with the time required to reach an equilibrium for the gas concentration . The delay before the slope of the concentration curve increases significantly depends on the flow rate of the inflowing gas. A higher flow rate results in a shorter dwell time, leading to a faster change in concentration inside the reactor, and vice versa. Therefore, the volume calculated by the reactor model depends on the set flow rate of the incoming gas by the MFC. To calculate the mass conversion rate described in Eq. 8, an accurate reactor model must be available. To determine the accuracy of the reactor model, several test with different flow rates were conducted.

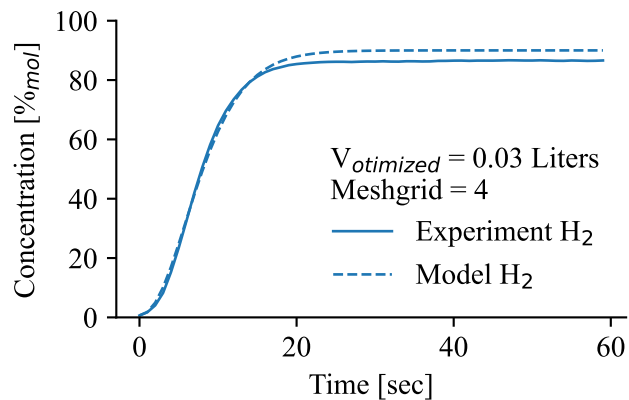


Fig. 32: Reactor model containing 4 CSTRs and an optimized volume

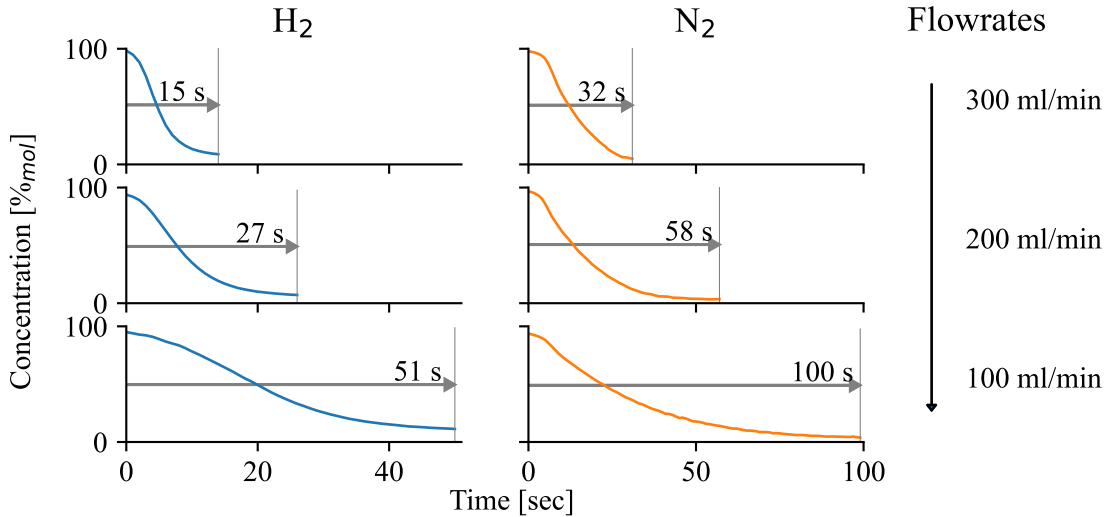


Fig. 33: Analysis of the diffusion time of N_2 and H_2 at different flowrates

To better understand the reactor model, the gas flow of each experiment was varied not only in terms of the flow rate but also regarding the gas itself. Experiments were conducted with an inflowing gas containing 100% N_2 and a reaction chamber pre-filled with 100% H_2 . The same was done with 100% H_2 in the inflowing gas and a reaction chamber pre-filled with pure 100% N_2 .

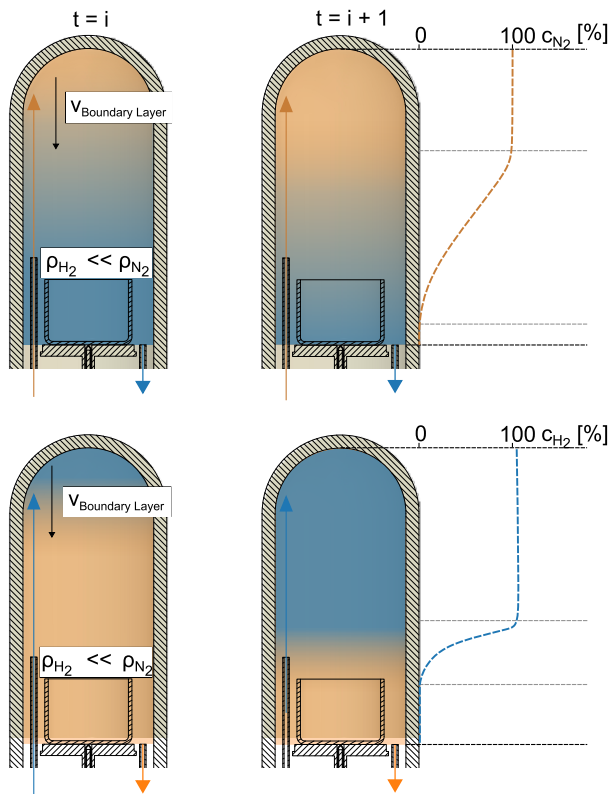


Fig. 34: Illustration of the factors affecting the convective transport of gases in the reaction chamber

The time required for the gas composition to reach equilibrium varied significantly across those experiments, not only in terms of the gas flow rate, but also regarding the gases itself. Switching from pure N_2 to H_2 goes nearly twice as fast compared to switching from N_2 to H_2 (Fig. 33). This behavior was observable for all tested gas flow rates. For both H_2 and N_2 , increasing the flow rate from 100 ml/min to 200 and 300 ml/min substantially reduces the time required to reach equilibrium. The notable difference switching from H_2 to N_2 compared to switching from N_2 to H_2 is probably caused by convection due to the different density of N_2 (1.251 kg/m^3) and H_2 (0.08987 kg/m^3) [34, 35]. Fig. 34 illustrates how the density of the gases influences the convective gas flow. In the figure, N_2 is represented in orange and H_2 in blue. The black arrow illustrates the speed of the boundary layer's movement, while the diagrams on the right side of the furnaces depict the concentration

changes within this layer. It shows a descending boundary layer due to convection, with the gases simultaneously diffusing into each other. The lower-density gas (H_2) more probably accumulates at the top of the furnace chamber, delaying its convective transport to the gas exit at the bottom of the furnace, because it tends to diffuse towards the top. In contrast, if H_2 flows into an N_2 atmosphere, the heavier N_2 is more prone to flow downwards, as it is the heavier of both gases. For this reason, the concentration gradient is much steeper in this setting. Therefore, the properties, especially the density of the gases plays a critical role, particularly in this setup with the reaction chamber being oriented vertically.

The gas concentration of the reactor model is difficult to estimate using a finite element method due to the complex diffusion behavior of the gases and the geometry of the furnace chamber. A model based on a computational fluid dynamic CFD simulation of the reaction chamber would be more appropriate, as it accounts for the different diffusion properties of the gases and the geometry of the furnace itself.

Additionally, the experimental campaign provided evidence that the gaseous zinc re-oxidizes on its way to the quartz capillary leading to the MS. The zinc reacts with the H_2O in the atmosphere, regenerating the consumed H_2 from the reduction of EAFD. This re-oxidation intensifies with higher H_2O concentrations in the gas flow. Therefore, the measured gas concentrations at the MS do not mirror the gas concentrations next to the EAFD specimen in the reaction furnace. The MS detects a higher H_2 concentration and a lower H_2O concentration. Thus, it is not possible to correlate the gas concentration signal of the MS with the mass signal of the TGA.

3 Summary and Outlook

Climate change poses one of the greatest challenges of the 21st century, driven by increased anthropogenic greenhouse gas emissions. Therefore, efforts are being made to reduce carbon dioxide emissions. The iron and steel industry is responsible for around 7.2 % of global carbon dioxide emissions. To reduce the carbon footprint of this industry, it is essential to recycle steel scrap. The primary recycling route for steel scrap is the Electric Arc Furnace EAF, which accounts for 28.9 % of world steel production. During steel recycling in the EAF, a high zinc-containing waste called Electric Arc Furnance Dust EAFD enters the exhaust gas and is extracted by bag filters. Per ton of produced steel, 15 to 23 kg of EAFD are generated, which results in a worldwide annual amount of 8.5 - 13 Mt. The zinc concentration in the EAFD, reaches up to 40 %, with an average concentration of around 20-25 %. This means that 1.7 - 3.3 Mt of zinc accumulate in EAFD each year. On the other hand, 13.5 Mt of zinc are produced per year. 60 % of this zinc is used for galvanizing steel, resulting in 8.1 Mt of zinc potentially contained in the steel currently produced. Therefore, once this scrap is recycled, zinc recovery from EAFD will become even more important in the future. The state-of-the art recycling process to recover zinc from EAFD is the Waelz process. Although efficient, the recovered zinc has a large carbon footprint because the zinc oxide in EAFD is reduced with carbon. European Green Deal forces the industry to implement mitigation measures including the transition from fossil carbon-based to sustainable, carbon-neutral production. In the scope of metallurgical reduction processes, hydrogen is often referred to as a promising solution.

The objective of this thesis was to investigate the hydrogen reduction behavior of EAFD in a Thermogravimetric Analyzer TGA at varying reaction temperatures and H_2O/H_2 ratios. To allow for safe operation, the reaction chamber was always kept at a slight overpressure to prevent any air infiltration. The gas flow rates were controlled using Mass Flow Controller MFCs. This setup was coupled with a Mass Spectrometer MS, which enabled detailed analysis of the reduction kinetics and the influence of temperature and gas atmosphere. Additionally, monitoring properties such as shrinkage behavior provided further insights into the reduction process. The TGA used was a customized Linseis STA PT1600, which allowed precise control of temperature and gas profiles. The experimental procedure consisted of a heating segment in an N_2 atmosphere, followed by an isothermal reduction using a reactive gas mixture of between H_2O and H_2 .

Cylindrical EAFD specimens were prepared through a pressing process and clinkered in a muffle furnace at 1000 °C to remove volatile components and enhance their mechanical stability. Then the specimens were placed in the reaction chamber of the TGA. A series of 32 experiments were conducted, with temperatures ranging from 900 °C to 1,200 °C, which are typical conditions in the Waelz kiln. The H_2O/H_2 ratio was adjusted from 0.0 (100 % H_2) to 1.2 (60 % H_2O and 40 % H_2). Reproducibility was ensured by maintaining consistent specimen mass and geometry and normalizing the reactive gas flow rates to account for slight changes in specimen mass. Calibration of the TGA weight measurements was performed by comparing the mass loss recorded by the TGA with the mass difference measured by a precision scale before and after reduction. Data from

the TGA and MS were collected at a frequency of 10 Hz and stored in a database. The raw data underwent cleaning and smoothing using various filters and numerical manipulation to prepare it for analysis. The mass loss and reduction kinetics were analyzed by calculating the mass loss rate and normalizing it with respect to the initial mass of each specimen, ensuring comparability.

The influence of temperature and H_2O/H_2 ratio on reduction kinetics and shrinkage behavior was systematically investigated. The reduction tests demonstrated that the shrinkage behavior of the specimens is significantly influenced by the reduction temperature. Higher temperatures resulted in greater shrinkage, although stagnating was observed above a temperature of 1,100 °C. Additionally, the mechanical stability of the specimens improved with higher temperatures due to enhanced sintering. The H_2O/H_2 ratio also affected shrinkage behavior, with higher H_2O content leading to increased shrinkage. As the iron oxide in the specimen reacts from hematite, over magnetite and wustite to metallized iron, the specimen contains phases with different melting points during the reduction process. Wustite has the lowest melting point of these compounds and tends to form mixed phases, such as fayalite, which has a melting point of 1,205 °C. This leads to the hypothesis, that the increase in shrinkage is due to the slower reaction kinetics and longer existence of the wustite with increased sintering behavior.

Reaction kinetics were primarily influenced by the temperature and the H_2O/H_2 ratio. Experiments with a higher temperature showed increased reaction rates up to 1,150 °C, beyond which the kinetics declined. Photos taken by the Digital Microscope DIMI showed, that when raising the temperature from 1,100 °C to 1,200 °C the shrinkage of the specimen declines, but the micropores transform to macropores. This may explain the low kinetics at 1,200 °C, as solid state diffusion becomes rate limiting.

At a H_2O/H_2 ratio of 0.0, the reaction kinetics increased by about 100 % when raising the reduction temperature from 900 °C to 1,150 °C. The maximum reaction kinetics after 5 % mass loss decreased by 30 %, when increasing the temperature to 1,200 °C. The H_2O/H_2 ratio also impacted the reaction kinetics, with higher ratios lowering it. At 1,000 °C, the maximum reaction rate decreased to around 40 % when the H_2O/H_2 ratio increased from 0.0 to 1.2.

In conclusion, both temperature and H_2O/H_2 ratio play critical roles in determining the reaction kinetics and shrinkage behavior of specimens during hydrogen reduction. A higher temperature generally enhances the reaction rate, but this is limited to a temperature of around 1,150 °C for the investigated material. On the other side, increased H_2O/H_2 ratios reduce reaction kinetics and, at high ratios, also the achievable reaction progress.

An additional objective of this thesis was to create a methodology to differentiate between the reduction of zinc and iron oxides in EAFD in order to train a neural network. Such a neural network would allow the estimation of the iron and zinc oxide reduction rates as a function of the process parameters.

This is done, by combining the H_2 consumption rate with the mass loss of the EAFD specimen during the reduction. The H_2 consumption rate is not directly measurable, because the MS just gives information about the gas composition. For this purpose, a gas model of the TGA reactor was developed and implemented using Python. The model calculates the gas composition as a function of the inflowing and generated gases in the reactor. However, the diffusive behavior of the gases in the reactor was too complex to be modeled via the finite element method. Experiments showed, that changing the gas from N_2 to H_2 takes half the time as the reverse direction from H_2 to N_2 . It appears, that H_2 accumulates at the top of the reactor, due to its lower density compared to N_2 , and pushes the N_2 to the outlet pipe at the bottom with less overlapping diffusion. Therefore,

the concentration shifts quite fast. On the other hand, when switching from N_2 to H_2 , more diffusion overlaps the convective gas flow, increasing the response time of the reactor. Additionally, during the experimental campaign, model development and experimental evaluation, it became obvious that distinguishing the reduction reactions of zinc and iron oxide is difficult. The issue is that gaseous zinc formed during the reduction of zinc oxide, re-oxidizes with water vapor between the specimen and the entry of the quartz capillary forming hydrogen. Therefore, the concentrations measured by the MS do not represent the actual concentrations in the reduction zone. From this perspective, it is not possible to combine the mass loss data from the TGA with the hydrogen consumption rate modeled using the measured gas composition from the MS.

Further investigation should address the current gap in experimental data, particularly by conducting experiments at 1,170 °C to achieve statistically more significant results. Additionally, it is also crucial to develop a methodology that can differentiate between the reduction reactions of zinc oxide and iron oxide.

Bibliography

- [1] Gunnar Myhre, Drew Shindell, Francois Bréon, Dongmin Lee, Belén Mendoza, Teruyuki Nakajima, Alan Robock, Graeme Stephens, Toshihiko Takemura, and Hua Zhang. “Anthropogenic and Natural Radiative Forcing”. In: *Climate Change 2013: The Physical Science Basis. Contribution of Working Group I to the Fifth Assessment Report of the Intergovernmental Panel on Climate Change*. Ed. by Thomas F. Stocker, Dahe Qin, Gian-Kasper Plattner, Michael Tignor, Simon K. Allen, Judith Boschung, Alexander Nauels, Yu Xia, Vincent Bex, and Paul M. Midgley. Cambridge, United Kingdom and New York, NY, USA: Cambridge University Press, 2013.
- [2] Hannah Ritchie and Max Roser. “CO₂ emissions”. In: *Our World in Data* (2020).
- [3] C. Fetting. “The European Green Deal”. In: *ESDN Report* (2020).
- [4] Jinsoo Kim, Benjamin K. Sovacool, Morgan Bazilian, Steve Griffiths, Junghwan Lee, Minyoung Yang, and Jordy Lee. “Decarbonizing the iron and steel industry: A systematic review of sociotechnical systems, technological innovations, and policy options”. In: *Energy Research & Social Science* 89 (2022), p. 102565. ISSN: 22146296. DOI: 10.1016/j.erss.2022.102565.
- [5] ArcelorMittal. *Hamburg H2: Working towards the production of zero-carbon emissions steel with hydrogen*. 2024. URL: <https://corporate.arcelormittal.com/climate-action/decarbonisation-technologies/hamburg-h2-working-towards-the-production-of-zero-carbon-emissions-steel-with-hydrogen>.
- [6] Energy Innovation Austria. *HYFOR®: Hydrogen-based Technology for Iron and Steel Production*. 2024. URL: <https://www.energy-innovation-austria.at/article/hyfor/>.
- [7] K1-MET GmbH. *SuSteel: Sustainable Steelmaking*. 2024. URL: https://www.k1-met.com/non_comet/susteel.
- [8] Salzgitter AG. *SALCOS® – Programm zur CO₂-armen Stahlproduktion*. 2024. URL: <https://salcos.salzgitter-ag.com/de/>.
- [9] thyssenkrupp Steel Europe AG. *Klimaneutraler Stahl - Unsere Strategie*. 2024. URL: <https://www.thyssenkrupp-steel.com/de/unternehmen/nachhaltigkeit/klimastrategie/klimastrategie.html>.
- [10] Zainul Abidin, Ali Zafaranloo, Ahmad Rafiee, Walter Mérida, Wojciech Lipiński, and Kaveh R. Khalilpour. “Hydrogen as an energy vector”. In: *Renewable and Sustainable Energy Reviews* 120 (2020), p. 109620. ISSN: 13640321. DOI: 10.1016/j.rser.2019.109620.
- [11] L. Barreto, A. Makihira, and K. Riahi. “The hydrogen economy in the 21st century: a sustainable development scenario”. In: *International Journal of Hydrogen Energy* 28.3 (2003), pp. 267–284. ISSN: 03603199. URL: <https://www.sciencedirect.com/science/article/pii/S0360319902000745>.

- [12] Leijiao Ge, Bohan Zhang, Wentao Huang, Yuanzheng Li, Luyang Hou, Jianbo Xiao, Zimu Mao, and Xiaoping Li. "A review of hydrogen generation, storage, and applications in power system". In: *Journal of Energy Storage* 75 (2024), p. 109307. ISSN: 2352-152X. DOI: 10.1016/j.est.2023.109307.
- [13] Jürgen Antrekowitsch, Gernot Rösler, and Stephan Steinacker. "State of the Art in Steel Mill Dust Recycling". In: *Chemie Ingenieur Technik* 87.11 (2015), pp. 1498–1503. ISSN: 0009-286X. DOI: 10.1002/cite.201500073.
- [14] Marja Rinne, Petteri Halli, Jari Aromaa, and Mari Lundström. "Alternative Method for Treating Electric Arc Furnace Dust: Simulation and Life Cycle Assessment". In: *Journal of Sustainable Metallurgy* 8.2 (2022), pp. 913–926. ISSN: 2199-3823. DOI: 10.1007/s40831-022-00531-x.
- [15] world steel association. "World Steel in Figures". In: (). (Visited on 03/21/2024).
- [16] Anne-Gwénaëlle Guézennec, Jean-Christophe Huber, Fabrice Patisson, Philippe Sessiecq, Jean-Pierre Birat, and Denis Ablitzer. "Dust formation in Electric Arc Furnace: Birth of the particles". In: *Powder Technology* 157.1-3 (2005), pp. 2–11. ISSN: 00325910. DOI: 10.1016/j.powtec.2005.05.006.
- [17] P. Oustadakis, P. E. Tsakiridis, A. Katsiapi, and S. Agatzini-Leonardou. "Hydrometallurgical process for zinc recovery from electric arc furnace dust (EAFD): part I: Characterization and leaching by diluted sulphuric acid". In: *Journal of hazardous materials* 179.1-3 (2010), pp. 1–7. DOI: 10.1016/j.jhazmat.2010.01.059.
- [18] Janaína Gonçalves Maria Silva Da Machado, Feliciane Andrade Brehm, Carlos Alberto Mendes Moraes, Carlos Alberto dos Santos, and Antônio Cezar Faria Vilela. "Characterization study of electric arc furnace dust phases". In: *Materials Research* 9.1 (2006), pp. 41–45. DOI: 10.1590/S1516-14392006000100009.
- [19] Elena Chirila and Cornelia Luca. "Fascicle of Management and Technological Engineering: Characterization of the electric arc furnace dust". In: *ANNALS of the ORADEA UNIVERSITY. Fascicle of Management and Technological Engineering* X.NR2 (2011).
- [20] V. N. Stathopoulos, A. Papandreou, D. Kanellopoulou, and C. J. Stournaras. "Structural ceramics containing electric arc furnace dust". In: *Journal of hazardous materials* 262 (2013), pp. 91–99. DOI: 10.1016/j.jhazmat.2013.08.028.
- [21] Sagar T. Cholake, Rifat Farzana, Taka Numata, and Veena Sahajwalla. "Transforming electric arc furnace waste into value added building products". In: *Journal of Cleaner Production* 171 (2018), pp. 1128–1139. ISSN: 09596526. DOI: 10.1016/j.jclepro.2017.10.084.
- [22] Mohammad A.T. Alsheyab and Taisir S. Khedaywi. "Effect of electric arc furnace dust (EAFD) on properties of asphalt cement mixture". In: *Resources, Conservation and Recycling* 70 (2013), pp. 38–43. ISSN: 09213449. DOI: 10.1016/j.resconrec.2012.10.003.
- [23] Natural Resources Canada. *Zinc Facts*. 2024. URL: <https://natural-resources.canada.ca/our-natural-resources/minerals-mining/mining-data-statistics-and-analysis/minerals-metals-facts/zinc-facts/20534>.
- [24] Gianluca Cusano, Miguel Rodrigo Gonzalo, Frank Farrell, Rainer Remus, Serge Roudier, and Luis Delgado Sancho. *Best Available Techniques (BAT) Reference Document for the Non-Ferrous Metals Industries*. EUR 28648 EN. Industrial Emissions Directive 2010/75/EU (Integrated Pollution Prevention and Control). Luxembourg: Publications Office of the European Union, 2017. ISBN: 978-92-79-69655-8. DOI: 10.2760/8224.

- [25] Andreas Ruh and Dae-Soo Kim. "The Waelz Process – Worldwide Most Used Process for the Recycling of Zinc Containing Residues". In: *EMC 2015*. Ratingen, Germany, 2015.
- [26] Pfeiffer Vacuum. *Mass Spectrometers and Residual Gas Analysis: Introduction & Operating Principle*. 2023.
- [27] Steven W. Smith. *The scientist and engineer's guide to digital signal processing*. 2. ed. San Diego, Calif.: California Technical Pub, 1999. ISBN: 0966017641.
- [28] Pauli Virtanen, Ralf Gommers, Travis E. Oliphant, Matt Haberland, Tyler Reddy, David Cournapeau, Evgeni Burovski, Pearu Peterson, Warren Weckesser, Jonathan Bright, Stéfan J. van der Walt, Matthew Brett, Joshua Wilson, K. Jarrod Millman, Nikolay Mayorov, Andrew R. J. Nelson, Eric Jones, Robert Kern, Eric Larson, C. J. Carey, Polat, VanderPlas, Jake, Denis Laxalde, Josef Perktold, Robert Cimrman, Ian Henriksen, E. A. Quintero, Charles R. Harris, Anne M. Archibald, Antônio H. Ribeiro, Fabian Pedregosa, Paul van Mulbregt, and SciPy 1.0 Contributors. "SciPy 1.0: Fundamental Algorithms for Scientific Computing in Python". In: *Nature Methods* 17 (2020), pp. 261–272. DOI: 10.1038/s41592-019-0686-2.
- [29] PubChem. *Ferrous oxide (FeO) CID 14945*. 2024. URL: <https://pubchem.ncbi.nlm.nih.gov/compound/14945>.
- [30] American Chemical Society. *Magnetite*. 2024. URL: <https://www.acs.org/molecule-of-the-week/archive/m/magnetite.html>.
- [31] PubChem. *Hematite (Fe2O3) CID 14833*. 2024. URL: <https://pubchem.ncbi.nlm.nih.gov/compound/14833>.
- [32] PubChem. *Iron (Fe) CID 23925*. Accessed: 2024-05-21. 2024. URL: <https://pubchem.ncbi.nlm.nih.gov/compound/23925>.
- [33] ChemicalBook. *Fayalite (Fe2(SiO4))*. 2024. URL: https://www.chemicalbook.com/ChemicalProductProperty_EN_CB9930861.htm.
- [34] PubChem. *Nitrogen (N2) CID 947*. 2024. URL: <https://pubchem.ncbi.nlm.nih.gov/compound/947>.
- [35] PubChem. *Hydrogen (H2) CID 783*. 2024. URL: <https://pubchem.ncbi.nlm.nih.gov/compound/783>.

List of Figures

1	Schematic illustration of the EAF [16]	2
2	Schematic representation of the burst of a bubble on a liquid surface [16]	3
3	Grain size distribution of EAFD	5
4	Flow chart of the Waelz process [25]	6
5	Picture of a pressed EAFD specimen taken by the DIMI	9
6	Overview of the experimental setup in the Linseis software of the TGA	10
7	Time dependent H_2 concentration with and without reaction	10
8	Illustration of the TGA	11
9	Effect of applying a moving average filter and a SavGol filter to the raw data of the TGA	12
10	Overview of data manipulation steps on the TGA data set	13
11	Reproducibility of the experiments in the TGA	14
12	Mass loss of the specimen during sample preparation	15
13	Influence of the reduction temperature on the shrinkage behavior of the specimens	17
14	DIMI pictures of the reduced EAFD specimen	18
15	Influence of the reduction temperature on the shrinkage behavior of the specimens	19
16	Volume loss of the specimen influenced by the H_2O/H_2 - ratio of the reactive gas	20
17	Overview of reaction kinetics of experiments with different process parameters	20
18	Temperature dependent reaction kinetics at a H_2O/H_2 ratio of 0.0	21
19	Temperature dependent reaction kinetics at a H_2O/H_2 ratio of 0.1	22
20	H_2O/H_2 ratio dependent reaction kinetics at a temperature of 1,000 °C	23
21	H_2O/H_2 ratio dependent reaction kinetics at a temperature of 1,150 °C	24
22	Diagram of H_2O production measured by the MS	25
23	Raw data of the mass deviation measured by the TGA	26
24	Calibration curves of the MS for H_2 , H_2O and N_2	28
25	Illustration of steam clogging in the quartz capillary	29
26	Change in gas composition of the reactor when switching from N_2 (orange) to H_2 (blue) without EAFD specimen.	30
27	Illustration of the functionality of the basic reactor model	31
28	Influence of the reactor volume V_{Reactor} on the H_2 concentration curve of the reactor model	32
29	H_2 concentration curve of the reactor model with the optimized volume $V_{\text{Reactor, optimized}}$	33
30	Influence of the number of CSTRs on the inertia of the H_2 concentration of the reactor model	34
31	Illustration of the implementation of CSTRs into the basic reactor model	34
32	Reactor model containing 4 CSTRs and an optimized volume	35
33	Analysis of the diffusion time of N_2 and H_2 at different flowrates	36

34	Illustration of the factors affecting the convective transport of gases in the reaction chamber	36
----	---	----

List of Tables

1	Composition of EAFD samples from a steel mill on eleven consecutive days [20]	4
2	Variation of process parameters across 32 experimental runs	8
3	Influence of the temperature on the different peaks of the reaction kinetic curve	22
4	Influence of the H_2O/H_2 ratio on the reaction kinetics	23
5	Influence of the H_2O/H_2 - ratio on the mass loss rate at 1,150 °C	24
6	Concentration set by the MFCs in order to determine a calibration curve for MS	27